

Investigating Corner-Frequency Uncertainties: Insights from Six Earthquakes (M_w 3.2–3.8) in Ridgecrest, California, and the Korean Peninsula

Minkyung Son^{*1} and Esteban J. Chaves²

ABSTRACT

Accurate corner-frequency (f_c) measurements are crucial for precise stress-drop ($\Delta\sigma$) estimates, essential for understanding earthquake mechanics and predicting ground motions, directly impacting seismic hazard assessments. This study investigated f_c variations for six earthquakes (M_w 3.2–3.8) across different tectonic regions: two from the 2019 Ridgecrest sequence in California (R1 and R2) and four from the Korean Peninsula—the 2022 Goesan mainshock (GM) and its foreshock (GF), the 2020 Haenam mainshock (HM) during a swarm-like sequence, and an aftershock (PA) of the 2017 Pohang earthquake¹. We employed the empirical Green's function approach, using cross-correlation coefficients (CCs) to select suitable Green's functions. We explored variations in frequency band, window length, and CC thresholds for cross-correlation, followed by deconvolution and spectral fitting. Our results indicate substantial differences in spectral shapes and f_c estimates among the six target events, reflecting diverse source characteristics: R1, R2, and GM (all M_w 3.8) exhibit distinct f_c distributions; PA (M_w 3.6) shows the most complex source time functions with one of the lowest f_c estimates. Variations in CC criterion and the upper bound of the frequency band used in the CC calculation significantly affected the mode and shape of the f_c estimate distribution for each target event, sometimes splitting the distribution into higher and lower f_c groups. We adjusted the variables to emphasize the low-frequency components, aiming to recover the overall structure of the source time function. This led to persistent differences in $\Delta\sigma$ estimates across the events, despite uncertainties Please change to 'in the individual fc estimates'. However, achieving this consistency was challenging without the adjustment, as errors Pelase change to 'in the fc estimates'. propagated on a cubic scale. Our findings provide a clear example that systematic f_c estimation can obscure stress-drop differences among events by increased uncertainties in $\Delta\sigma$ estimates for individual events, especially with different tectonic settings and source complexities.

KEY POINTS

- Spectral shapes and source time functions (STFs) of six M_w 3.2–3.8 earthquakes did not show the same pattern.
- Changes in upper band limits for cross-correlation coefficient (CC) and CC criteria in empirical Green's function (EGF) selection lead to large variations in f_c estimates.
- Low-frequency contents in EGF approaches are critical for capturing variation in stress drops across events.

Supplemental Material

the event, to a steep (or high-frequency) decay, which is generally proportional to f^{-2} (e.g., Aki, 1967; Abercrombie, 2021). Understanding and accurately measuring f_c is essential, as attenuation models, which are used to predict ground motion, are highly dependent on this parameter (Ji and Archuleta, 2021). These models are foundational for creating seismic hazard

1. Earthquake Research Center, Korea Institute of Geoscience and Mineral Resources, Daejeon, Republic of Korea, <https://orcid.org/0000-0003-4862-8510> (MS);
2. Volcanological and Seismological Observatory of Costa Rica, OVSICORI, Universidad Nacional, Heredia, Costa Rica, <https://orcid.org/0000-0002-5724-1513> (EJC)

*Corresponding author: kersti@kigam.re.kr

Cite this article as: Son, M., and E. J. Chaves (2025). Investigating Corner-Frequency Uncertainties: Insights from Six Earthquakes (M_w 3.2–3.8) in Ridgecrest, California, and the Korean Peninsula, *Bull. Seismol. Soc. Am.* **XX**, 1–23, doi: [10.1785/0120240149](https://doi.org/10.1785/0120240149)

© Seismological Society of America

maps, employed by engineers, urban planners, and policymakers to design safer buildings and prepare for future earthquakes.

As shown in multiple studies (e.g., Brune, 1970; Boatwright, 1978), f_c is directly related to the size and dynamics of the earthquake source, providing essential information about the rupture process, including the size of the fault area that slipped and the earthquake stress drop ($\Delta\sigma$):

$$\Delta\sigma = \frac{7}{16} \frac{M_0}{r^3}. \quad (1)$$

Equation (1) shows that, for the same M_0 , stress drop varies inversely with the cube of the rupture radius r , which is expressed as (e.g., Brune, 1970; Madariaga, 1976):

$$r = \frac{k\beta}{f_c}, \quad (2)$$

in which f_c is the corner frequency, β is assumed to be proportional to rupture velocity, and k represents rupture characteristics (Kaneko and Shearer, 2014; Ji and Archuleta, 2021).

Thus, variations in the assumed values for k and β , as well as in the estimates for f_c , can lead to significant differences in stress-drop estimates. For instance, switching from Madariaga's k for S waves (0.21; Madariaga, 1976) to Brune's (0.372) results in a stress-drop decrease by a factor of ~ 5.5 , due to an increase in rupture radius. In addition, errors in estimating f_c , which propagate cubically when calculating stress drops (as shown in equations 1 and 2), can introduce substantial discrepancies in stress-drop estimates. These discrepancies can significantly hinder our understanding of earthquake mechanics. Therefore, it is crucial to ensure precise measurement of f_c and a thorough understanding of the associated parameters to prevent significant error propagation. Such efforts have far-reaching implications for both scientific research and practical applications in earthquake hazard mitigation.

The 2022 Goesan earthquake (M_w 3.8; GM) and its largest foreshock (M_w 3.2; GF) in the central Korean Peninsula (Fig. 1a, Table S1, available in the supplemental material to this article) exemplify the challenges in estimating corner frequencies and stress drops (Table 1). Recently, Kim *et al.* (2023) reported 84 MPa for GM and 107 MPa for GF, whereas Lim *et al.* (2024) computed 29 MPa for GM. The temporal proximity of GF to GM, with GF occurring only ~ 17 s before GM, caused limitations in selecting stations and frequency bands, despite both studies using different methods for the estimation. Kim *et al.* (2023) employed an empirical Green's function (EGF) approach for S waves, based on Boatwright's source model (Boatwright, 1978), whereas Lim *et al.* (2024) used Brune's source model (Brune, 1970) to fit displacement spectra of S wave. The f_c estimates of both studies differ, and variations in the selections of the values for both k and β , described in equation (2), increased the discrepancy in the stress-drop estimates (Table 1).

Despite the potential variation or uncertainty in estimates of corner frequencies and stress drops, these source parameters

provide insight into fundamental questions, such as the hypothesis of earthquake self-similarity, and practical applications, like predicting strong ground motions. Several methods have been proposed throughout the decades (e.g., Mayeda and Walter, 1996; Abercrombie, 2014; Uchide and Imanishi, 2016) and applied to various seismic events, aiming to maintain a consistent or objective procedure across earthquakes or seismic events in different tectonic regions (e.g., Morasca *et al.*, 2022). Recently, there have been a different approach, which is the Southern California Earthquake Center (SCEC)/U.S. Geological Survey (USGS) Community Stress-Drop Validation Study led by Baltay *et al.* (2024). It incorporates a variety of methods for earthquake source parameter estimations, but focusing on a common dataset of the 2019 Ridgecrest, California, earthquake sequence (Trugman, 2020) to explore the uncertainty in source parameter estimates.

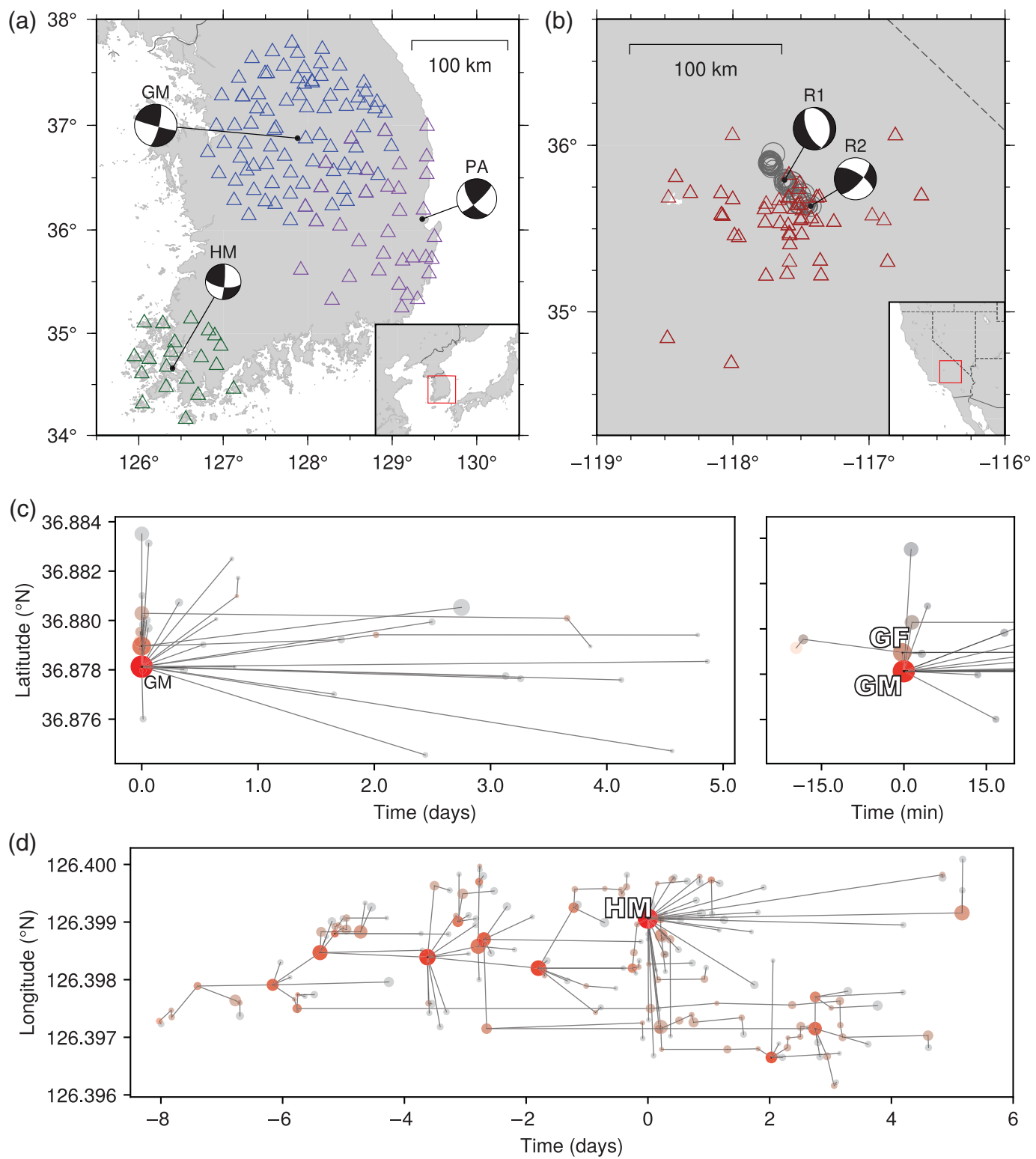
In this work, we investigate potential variations in f_c estimates, using the EGF approach that considers only a cross-correlation coefficient (CC) for selecting suitable Green's functions for a target event. We illustrate a workflow for EGF selection, deconvolution, and spectral fitting, specifying optional procedures such as normalization and averaging, and variables such as the number of tapers and resampling rate. We then iterate the entire workflow, varying frequency band (lower limit f_{low} and upper limit f_{high}) and window length ($nsec$) used in computing CC, and the CC criterion (CC_{cut}) for EGF selections. This approach would provide insight into how systematic f_c estimations behave with respect to frequency band or window length, which are usually determined by earthquake magnitude (e.g., Abercrombie *et al.*, 2017) or epicentral/hypocentral distance to stations (e.g., Kim *et al.*, 2023).

We target six earthquakes with M_w ranging from 3.2 to 3.8. We refer to them as GM, GF, R1, R2, PA, and HM (Table 1, Table S1). Figure 1a,b shows their epicentral location. R1 and R2 are both M_w 3.8 earthquake, like GM, and are cataloged in the open dataset of 55 events selected for the SCEC/USGS stress-drop validation study (Fig. 1b; Trugman, 2020; Baltay *et al.*, 2024). PA is one of the largest aftershock in the fault segment where the 2017 Pohang, Korea, earthquake occurred, with a hypocentral distance of 0.97 km to the Pohang main-shock (M_w 5.4), highlighting its proximity to the fluid injection point (Fig. 1a; Son *et al.*, 2020). HM is the largest event of the 2020 Haenam earthquake sequence, an event located along the southwestern section of the Korean Peninsula (Fig. 1a; Son *et al.*, 2021), known for its low seismicity rate. A swarm-like behavior of the 2020 Haenam sequence contrasts with the 2022 Goesan earthquake sequence, characterized by the event GF as a foreshock (Fig. 1c,d; Text S1).

METHODS

EGF approaches based on a CC

We applied a spectral ratio fitting method based on EGF approaches (Abercrombie *et al.*, 2017; Ruhl *et al.*, 2017;



Chaves *et al.*, 2020) to separate earthquake source effects from attenuation effects recorded on the vertical components (P waves). Generally, this approach utilizes the seismogram of a smaller, colocated earthquake to represent the path and site effects in a larger earthquake. Thus, the earthquake catalogs of each sequence serve as an EGF candidate set. We used all cataloged events with magnitudes at least 0.4 smaller than the

Figure 1. Target event information: maps for events (a) GM (M_w 3.8), PA (M_w 3.6), HM (M_w 3.2) in the Korean Peninsula; (b) R1 (M_w 3.8) and R2 (M_w 3.8) in the Ridgecrest area, California; earthquake family plots for (c) GM and (d) HM. The triangles denote the stations used in this study. (c, d) Earthquake family plots for GM and HM, respectively, where circles correspond to earthquakes, and lines indicate parent links. Text S1 in the supplemental material describes details on the declustering results. All the catalogs are from Lim *et al.* (2024), Son *et al.* (2020, 2021), and Trugman (2020).

TABLE 1

Published Information of the Target Earthquakes (GM, GF, R1, R2, PA, and HM)

ID	Reference	Magnitude (M_w)	f_c (Hz)	k	β (km/s)	$\Delta\sigma$ (MPa)	Note
GM	Kim	3.8 (Brune)	5.6 (EGF; S)	0.21 (Mada.; S)	3.6 (3.5*)	84	Std. of f_c , 0.8 Hz
	Lim	3.8 (TDMT)	3.6 (Brune; S)	0.37 (Brune; S)	3.5	29	$M_{w,TDMT}$ used in this study
GF	Kim	3.5 (Brune)	8.1 (EGF; S)	0.21 (Mada.; S)	3.6 (3.5*)	107	Std. of f_c , 0.4 Hz
	Lim	3.3 (TDMT)	—	—	—	—	$M_{w,TDMT}$ used in this study
R1	Trugman	3.8 (SCEDC)	5.1 (SD; P)	0.38 (K&S; P)	3.52	12	M_w used in this study
R2	Trugman	3.8 (SCEDC)	3.3 (SD; P)	0.38 (K&S; P)	3.52	8.44	M_w used in this study
PA	Son1	3.6 (TDMT)	—	—	—	—	$M_{w,TDMT}$ used in this study
HM	Sheen	3.2 (Brune)	3.8 (Brune; S)	0.37 (Brune; S)	3.86	3.1	Std. of f_c , 0.1 Hz
	Son2	3.2 (TDMT)	—	—	—	—	$M_{w,TDMT}$ used in this study

Brune, Brune (1970); EGF, empirical Green's function; ID, event identifier; K&S, Kaneko and Shearer (2014); Kim, Kim et al. (2023); Lim, Lim et al. (2024); Mada., Madariaga (1976); P, P wave; S, S wave; SCEDC, Southern California Earthquake Data Center; Sheen, Sheen (2021); SD, spectral decomposition (Trugman and Shearer, 2017); Son1, Son et al. (2020); Son2, Son et al. (2021); Target, Chosen due to available M_w estimated by TDMT when multiple references are available; TDMT, time-domain moment tensor inversion (Dreger, 2003); Trugman, Trugman (2020).

*3.5 km/s used in M_w estimation in Kim et al. (2023).

TABLE 2

Number of Empirical Green's Function (EGF) Candidates and Station Details for the Target Earthquakes

Dataset/Target Events	GM	PA	R1	R2	GF	HM
Number of EGF candidates	41	867	31	30	40	226
Number of stations	85	38	38	53	85	20
Maximum distance from target to stations (km)	100	150	130	130	100	80

target event's magnitude as EGF candidates (Table 2). Specifically, we employed the catalog from Lim et al. (2024) for GM and GF, the catalog from Son et al. (2021) for HM, a subset of the catalog from Son et al. (2020) for PA in the fault segment of interest, and the subset catalog compiled for the SCEC/USGS stress-drop validation study (Baltay et al., 2024) from Trugman (2020), for R1 and R2. For the target events in the Korean Peninsula (i.e., GM, GF, PA, and HM), we prioritized the local magnitude scale in our magnitude difference comparison, as most EGF candidate events lacked moment magnitude information: for GM, GF, and PA, we used the catalogs of the Korea Meteorological Administration; for HM, Son et al. (2021).

Caution is needed when comparing f_c estimates obtained from different methods (Shearer et al., 2019; Calderoni and Abercrombie, 2023). This also applies to the EGF approach, as EGF selection can depend on factors such as hypocentral distances, focal mechanisms, magnitude differences, and CCs. In this study, we used CCs as the sole criterion for selecting EGFs at each station, as waveform similarity may reflect similarity in earthquake hypocenter location and faulting mechanism. This approach reduces the number of choices during EGF selections and provides EGFs that are aligned to the target waveform by each lag time. We computed CC between each EGF candidate record and a target (i.e., GM, GF, HM, PA, R1, and R2) recorded at 100 Hz by the corresponding seismic station networks shown in Figure 1a,b. Stations were excluded based on shear-wave

velocity (Table 1) for each window length used to avoid S-phase contamination. We used the velocity-broadband seismometer when both a velocity sensor and an accelerometer were available; otherwise, we used the accelerometer record. The following section describes the process of obtaining the CC in detail, after introducing the variables used in the CC calculation.

Testing various frequency bands and window lengths for CC

A frequency band and window length applied to seismograms of the event pair can vary CC, often resulting in differences in the selected EGF sets or the parts of the signals to be used. We explored variations in f_c estimates according to a CC criterion (CC_{cut}) used in EGF selections and changes in the frequency band (lower limit f_{low} and upper limit f_{high}), as well as window length ($nsec$) used in computing CC (Table 3; see the “X-correlation” part in the gray in Fig. 2). We tested the parameters in set A (Table 3), after designing the set to cover a wide range. For example, set A includes the ranges derived from the formula proposed by Abercrombie et al. (2017): an f_{low} of 0.5, an f_{high} range of 2.3–4.8, and an $nsec$ range of 2.1–4.3. These f_{high} and $nsec$ values roughly correspond to the inverse of source duration and its ten times estimates for earthquakes with M_w ranging from 3.2 to 3.8, assuming a low stress-drop condition (~ 0.1 MPa; Abercrombie et al., 2017).

Figure S1 illustrates an example result for determining the maximum value of the CCs and the corresponding lag time

TABLE 3

Sets of Variables Used in Computing CC for Empirical Green's Function (EGF) Selections: Frequency Bands from f_{low} to f_{high} with Window Lengths of $nsec$, Along with a CC Criterion of CC_{cut}

ID	f_{low} Coefficients Paired with f_{high}	f_{high} (Hz)	$nsec$ (s)	CC_{cut}
Set A	<0.04, 0.4, 4> at 0.04 constant	<1.0, 5.0, 5>	[2.1, 5.1, 0.6]	[0.60, 0.90; 0.10]

The notation “ a, b, c ” signifies a logarithmically spaced range from “ a ” to “ b ,” where “ c ” denotes the number of evenly distributed samples within the interval. The notation “[a, b, c]” denotes a range from “ a ” to “ b ” with values spaced evenly by “ c .” For example, one f_{high} generates four frequency bands in set A, starting with 0.04 (anchored), 0.09 f_{high} , 0.19 f_{high} , and 0.4 f_{high} Hz.

between an EGF candidate and a target. We used signals starting 1 s before the P picks to capture the onset of P arrivals and contrast them from the preceding noise. The signals continued up to $nsec$ after P pick. We set the lag time to range from −1.0 to 1.0 s to adjust the theoretical P picks applied to EGF candidates for GM, GF, PA, and HM events. This lag limit was also applied to the R1 and R2 events and their EGF candidates to adjust the P picks listed in the SCEDC phase files. We obtained the maximum CC value and its corresponding lag time using *xcorr_pick_correction* in ObsPy (Krischer et al., 2015). The time series of the concave region containing the maximum CC was fitted to a quadratic equation using *scipy.polyfit* (Virtanen et al., 2020) to achieve submillisecond resolution.

Spectral ratio fitting and source time function recovery

Figure 2 illustrates the workflow for deconvolution and spectral fitting, indicating optional procedures within square brackets “[]” and variables marked in italic. We obtained the spectra of the vertical component for the target and each EGF using MTSpec in *multitaper*, an open-source Python package of Prieto (2022), with seven tapers. Next, we resampled the spectra at intervals of 0.06 Hz on a logarithmic scale and computed spectral ratios between the target and each EGF for each station. We then normalized the individual ratios, averaged them across all EGF for each station, and normalized the averaged ratio again. This normalized spectral ratio, with a maximum amplitude of 1, served as the observed spectral ratio for each station available in our study for each target event. Figure S2 shows an example of interim results for an individual station.

The normalized spectral ratio between the two events, “Target” and “EGF” (i.e., large and small earthquakes, respectively), can be modeled as follows:

$$\frac{M_{\text{Target}}(f)}{\dot{M}_{\text{EGF}}(f)} / A = a \left(\frac{1 + (f/f_{c,\text{EGF}})^4}{1 + (f/f_{c,\text{Target}})^4} \right)^{1/2}, \quad (3)$$

assuming the sharper-cornered model of Boatwright (1978). Here, the seismic moment ratio term, A , corresponds to $\dot{M}_{0,\text{Target}}/\dot{M}_{0,\text{EGF}}$, when the normalized long-period spectral level, a , equals 1. We fitted the observed spectral ratio for each station, obtained through the averaging and normalizing

procedures described above, to equation (3) with the variables, a , $f_{c,\text{EGF}}$, and $f_{c,\text{Target}}$.

We utilized the Levenberg–Marquardt algorithm from the LMFIT Python package by Newville et al. (2022) for curve fitting, obtained an f_c estimate of the target for each station, but excluded stations where the modeled long-period amplitude was smaller than 0.5, idealized as 1. This exclusion is the only selection procedure applied to the observed spectral ratio for each station. Across the stations that remained after this selection, we averaged the observed spectral ratios and normalized the averaged ratio. Fitting this final spectral ratio to equation (3) yielded an f_c estimate of the target.

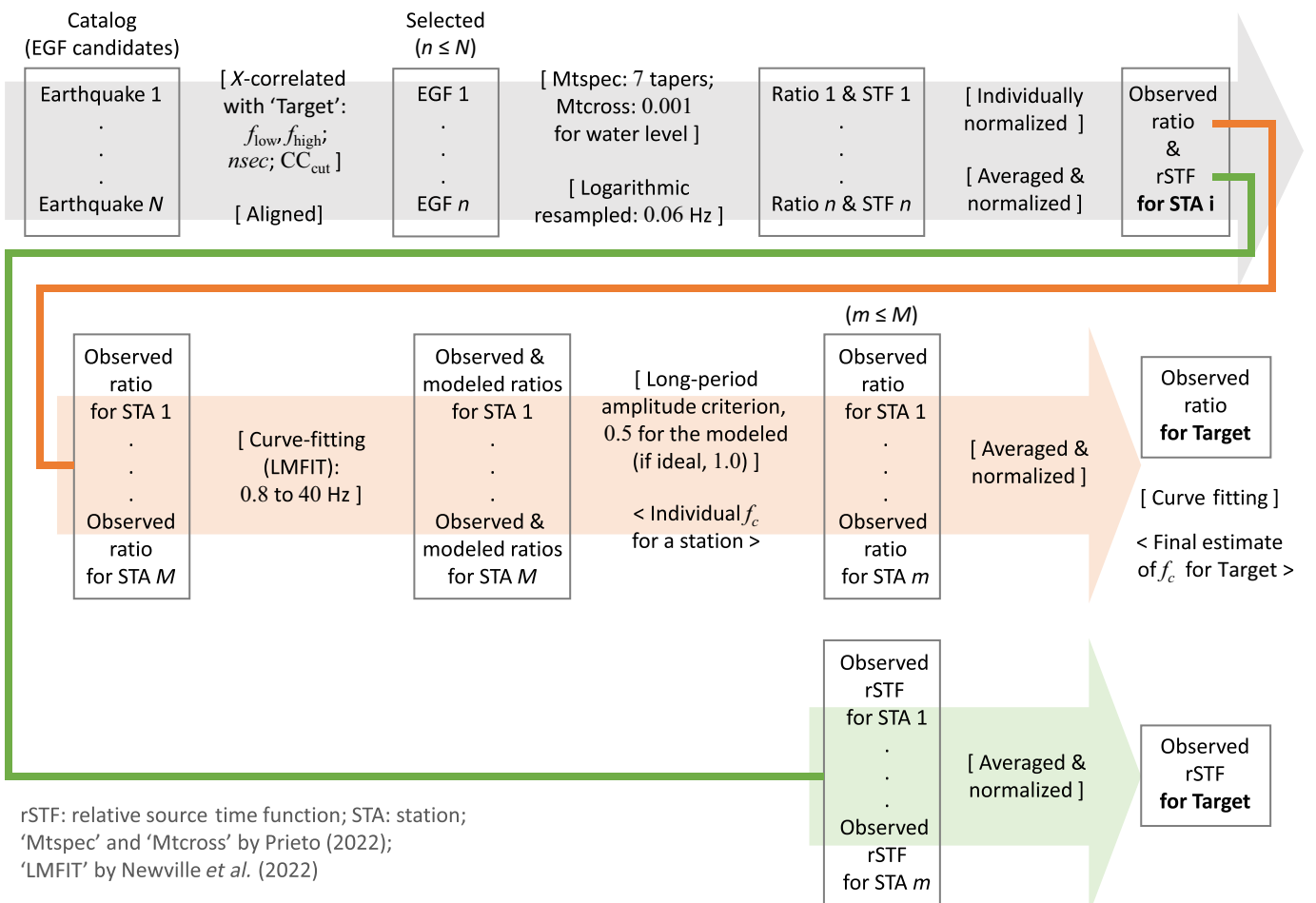
MTCross, part of the same *multitaper* package, computed individual cross spectra between the target and each EGF event with a water level of 0.001. This procedure generated an individual time-domain source time function (STF) for each EGF at each station. At each station, we normalized these individual STFs, averaged them across all EGFs, and then normalized the averaged function again. Each station’s averaged STF served as the relative source time function (rSTF). We then averaged the rSTFs across the stations selected during spectral fitting. After normalizing the average, we obtained the final single trace: the rSTF for the target.

RESULTS

Variations in f_c estimates and source durations

The combination of variables generated by set A allowed us to produce 480 EGF selection conditions per event, meaning that the number of f_c estimates, spectral ratios, and STFs could each reach up to 480 per event. In this study, we considered an f_c estimate valid when it was averaged from four or more stations. Consequently, we obtained 473, 338, 298, 326, 452, and 309 deconvolution results for the six target events—GM, R1, R2, PA, GF, and HM, respectively. The general trend in the obtained spectral ratios for the six target events varies significantly in the shapes of their long-period amplitudes and fall-off (see the first column of Fig. 3), even though their corresponding seismic moments are similar.

A common observation across the six target events is that the reciprocals of f_c estimates frequently appear smaller than the expected durations inferred from the observed shapes of the STFs (see the second column of Fig. 3). The f_c estimates are distributed over a wide frequency range spanning several

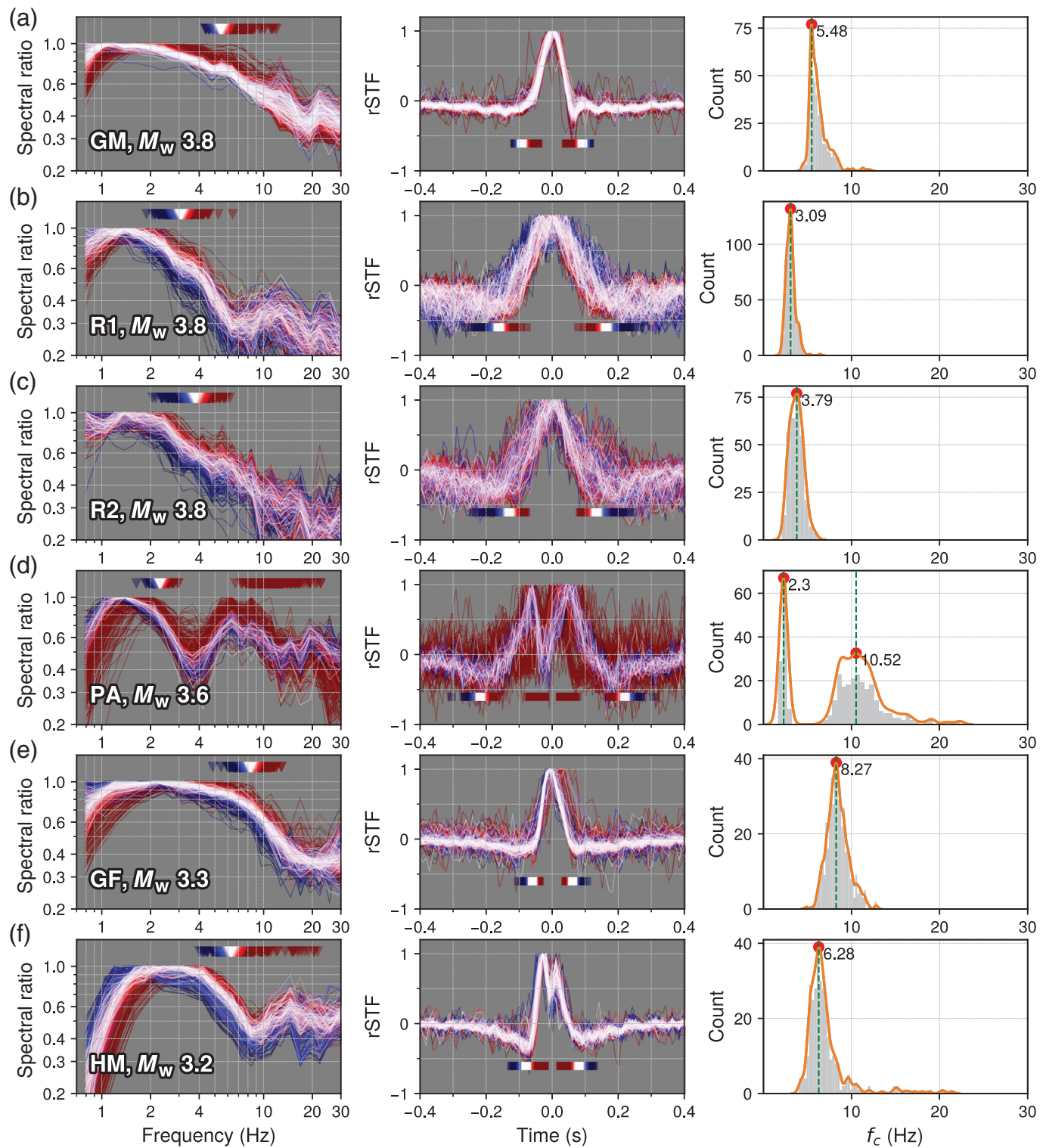


Hertz (see the third column of Fig. 3). Specifically, the f_c computed from the spectral ratios for GM consistently appear at higher frequencies (Fig. 3a), compared to those for R1 and R2 (Fig. 3b,c), despite all three earthquakes having the same moment magnitude (M_w 3.8). These differences in f_c estimates, along with variations in focal mechanisms and source regions (Fig. 1), suggest that earthquake source characteristics, including f_c , may be influenced by faulting style or mechanical properties along the fault. However, the limited number of events in this comparison restricts the depth of discussion, warranting further studies to explore this observation.

The target event, PA with a magnitude of M_w 3.6, smaller than GM, R1, and R2, shows one of the most complex sources in both time and frequency domains compared to the rest of the events. This complexity resulted in one of the lowest f_c estimates in this study (Fig. 3d). For the spectral ratios of PA, the long-period amplitudes reveal two distinct bumps, which makes two separate groups in f_c estimates, as shown in the first panel of Figure 3d. For GF, the high f_c estimate group also suggests a shorter duration than expected based on visual inspection of the rSTFs (see the red markers in Fig. 3e). For HM, the reciprocals of the high f_c estimates deviate from the expected durations, particularly for the doublet in the rSTFs (Fig. 3f).

Figure 2. Workflow for spectral ratio fitting and source time function (STF) recovery using empirical Green's function (EGF) approaches and cross-correlation coefficients (CCs): "Catalog" lists N seismic events with magnitudes smaller than that of the "Target." The procedures enclosed in "[" and "]" may vary between studies. The color version of this figure is available only in the electronic edition.

The events predominantly used as EGFs can be identified in Figure 4a, which depicts the relative hypocenter distance and magnitude difference between each EGF and the target. The events frequently used are spatially close to each target, especially for GM, PA, GF, and HM, as shown in Figure 4a and Table S2. Interestingly, PA and HM, which have a complex STF (Fig. 3d,f), utilize the largest number of EGFs for deconvolution. For R1 and R2, the most frequently used EGFs are the first and second closest events from each target, as illustrated in Figure 4a. However, some events located tens of kilometers away from each target were also utilized as EGFs, challenging the assumption that EGFs must be "collocated seismic events." This indicates that high CC values alone do not guarantee the EGF assumption for R1 and R2, due to several factors, such as cycle-skipping caused by a long lag limit when computing the maximum CC values (e.g., Schaff *et al.*, 2004).



It is noteworthy that the GM, PA, GF, and HM events are the mainshock or one of the largest-magnitude events in each sequence, whereas R1 and R2 are part of the aftershock sequence of the two Ridgecrest earthquakes (M_w 6.4 and 7.1; Trugman, 2020). Thus, the catalog we considered for EGF candidates for R1 and R2 covers a spatially wide-ranging area. This suggests that the EGF selection strategy based solely on CC

Figure 3. Normalized spectral ratios, relative source time functions (rSTFs; not filtered), and f_c estimate distributions for (a) GM; (b) R1; (c) R2; (d) PA; (e) GF; and (f) HM, generated by iterations of the workflow in Figure 2 with set A in Table 3. Markers in the first and second columns represent an f_c estimate and a pair of \pm half of its reciprocal, respectively, with the mode of f_c estimate denoted in white. Event identifiers and related information can be found in Table 1 and Table S1.

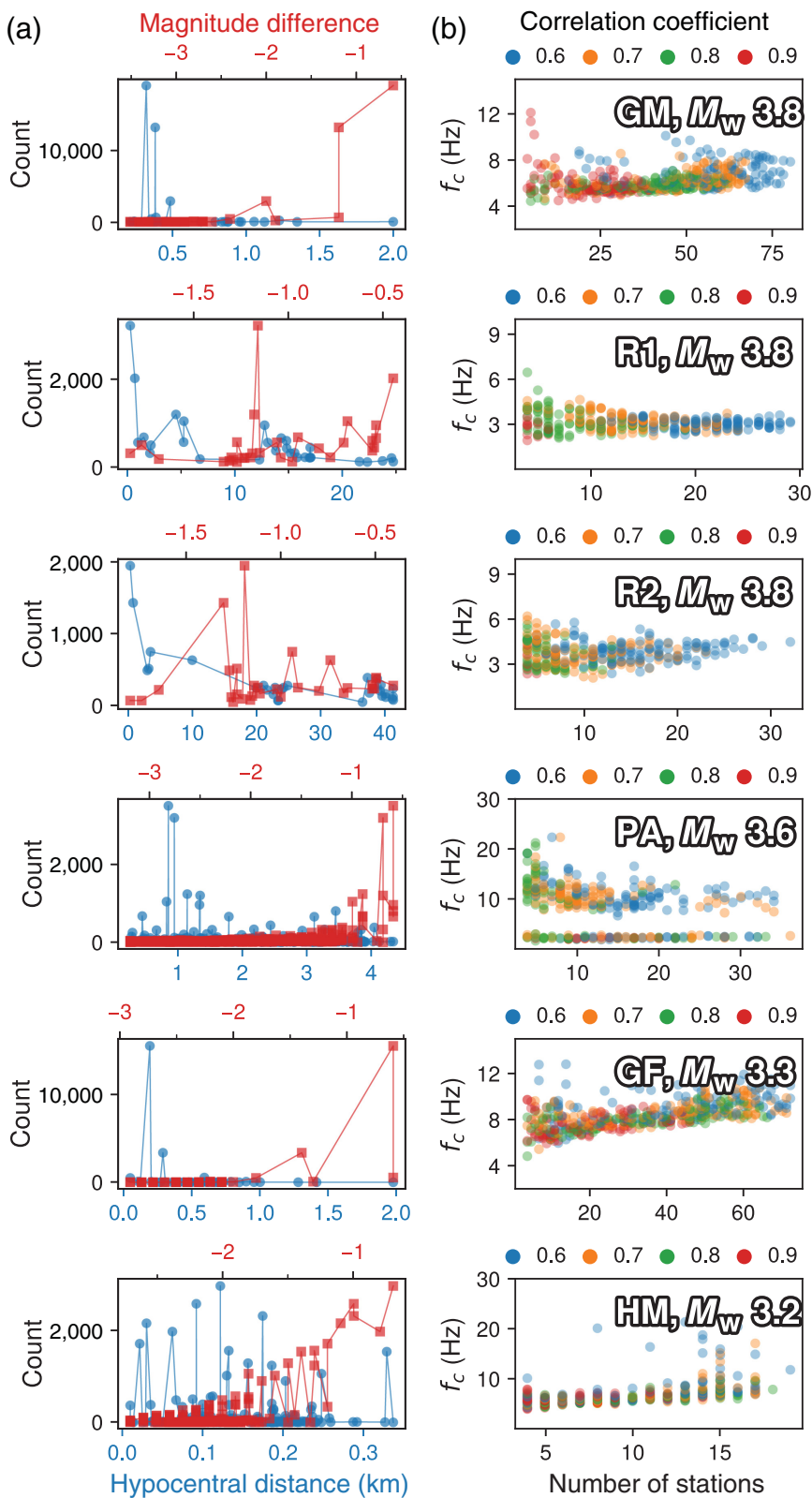
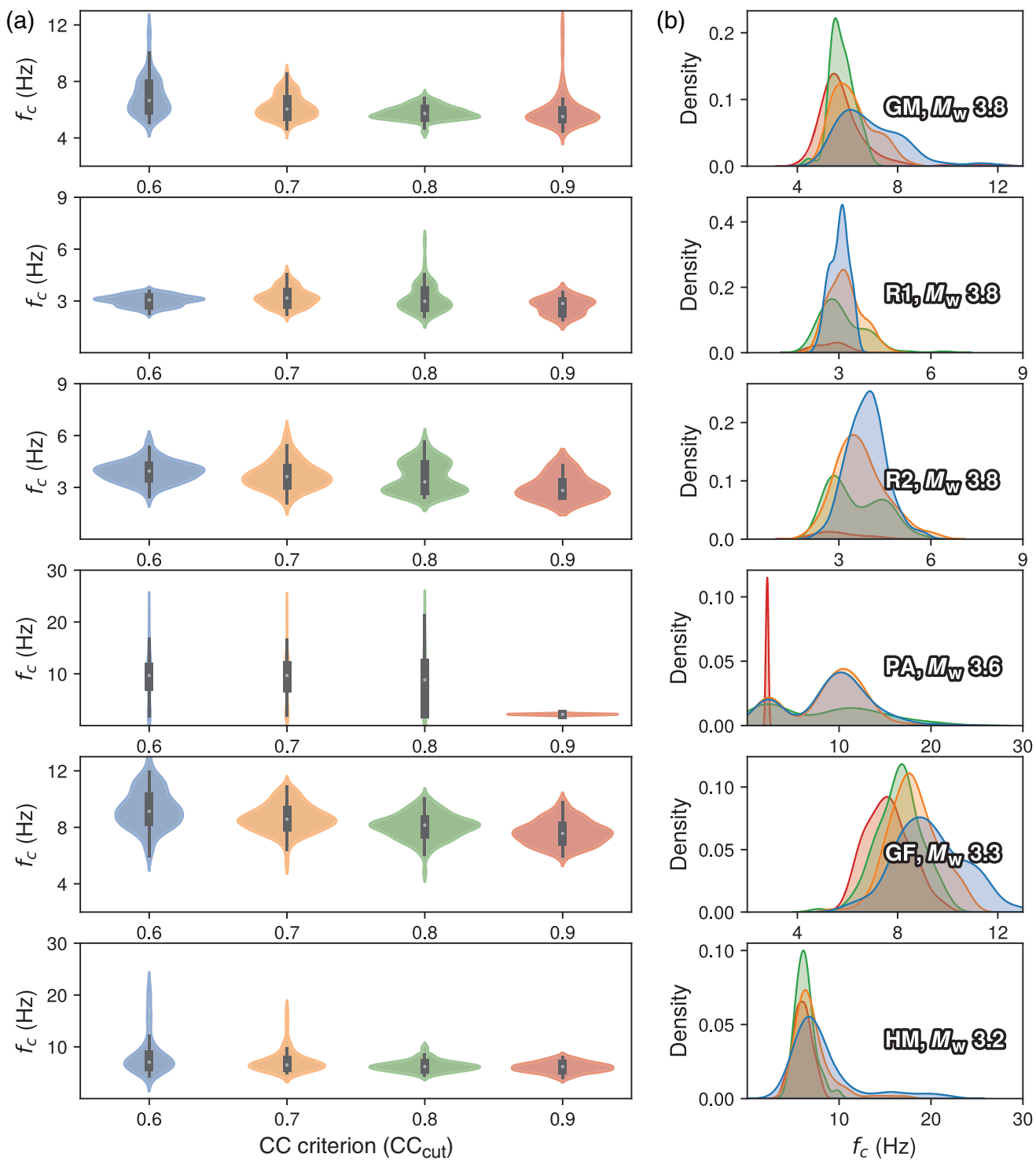


Figure 4. Information on selected EGFs and stations: (a) frequency of each EGF's usage, including hypocentral distance to the target and magnitude differences for each EGF; (b) variations in the number of stations used, categorized by CC_{cut} for EGF selections. Each circle represents the corner-frequency distribution resulting from the deconvolution of the target event.

could be valid for deconvolutions of the largest-magnitude events in an earthquake sequence without the need for tailoring the catalog. However, for most events that are not the mainshock or the largest in a sequence, a preliminarily tailored catalog with additional criteria, such as magnitude difference or hypocentral distance between the target and an EGF candidate, or some criteria that could serve as alternatives, would still be needed.

In terms of magnitude differences between an EGF and the target, deconvolutions for GM, PA, GF, and HM mainly utilized events with magnitudes very close to the target events (see the top-right square for the minimum magnitude differences in Fig. 4a). This selection occurred because events with smaller magnitude differences tend to have higher CCs, as documented by previous studies (Waldhauser and Schaff, 2008; Son *et al.*, 2015). For the same reason, in the deconvolution results for R1 and R2, events with magnitudes close to the target (difference level < 0.5) were frequently selected due to their higher CC values.

Furthermore, the number of stations used inversely correlates with CC_{cut} used in deconvolutions for GM, R1, R2, and PA (Fig. 4b, Fig. S3), presenting a trade-off between the number of stations and CC_{cut} . In addition, CC_{cut} affects f_c estimate distributions (Fig. 4b), though this effect is event-specific. For example, GM shows a trend where f_c estimates have a sharper distribution with a high CC_{cut} value of 0.8, unlike R1, R2, and PA. In the case of HM, due to the smaller number of stations, clear trends with



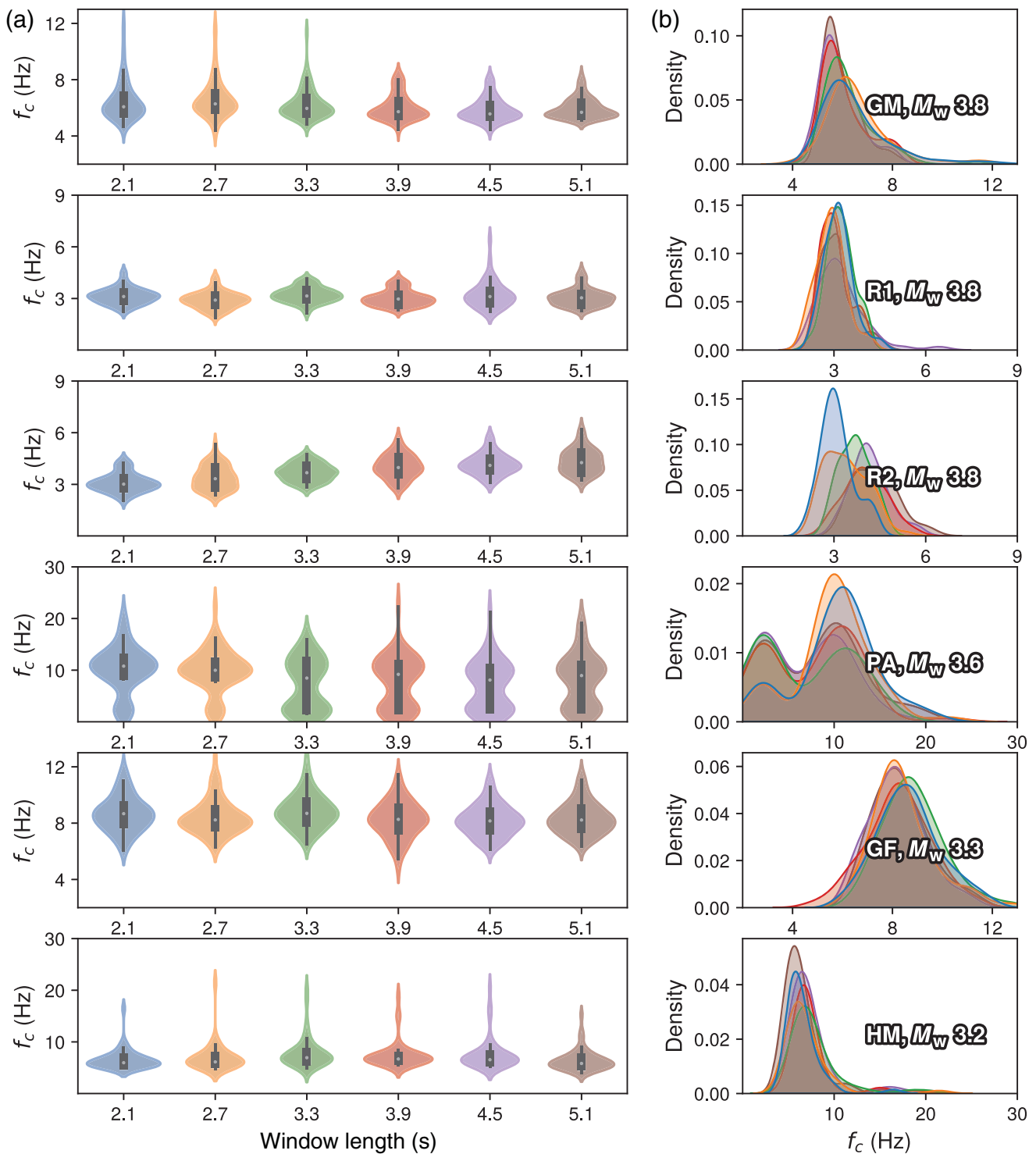
CC_{cut} are difficult to determine; however, we notice that with 5–13 stations, f_c estimate distributions are less diverse (Fig. 4b).

Event-specific f_c sensitivities by input variables

The CC criterion for EGF selections, CC_{cut} , affected f_c estimate variations (Fig. 5). It is evident that higher CC_{cut} lowers the mode of f_c distributions. The shapes of f_c estimate distribution plots differ even within a single event. It is difficult to identify a

Figure 5. Variations in f_c estimates according to CC_{cut} , a CC criterion to select EGF: (a) violin plots (normalized distributions) for CC_{cut} in set A; (b) plain distribution curves with the same details as those in panel (a).

clear trend across events, but f_c estimate distributions for R1 and PA show modes and shapes that differ significantly from those at other CC_{cut} values. On the other hand, $nsec$, the length

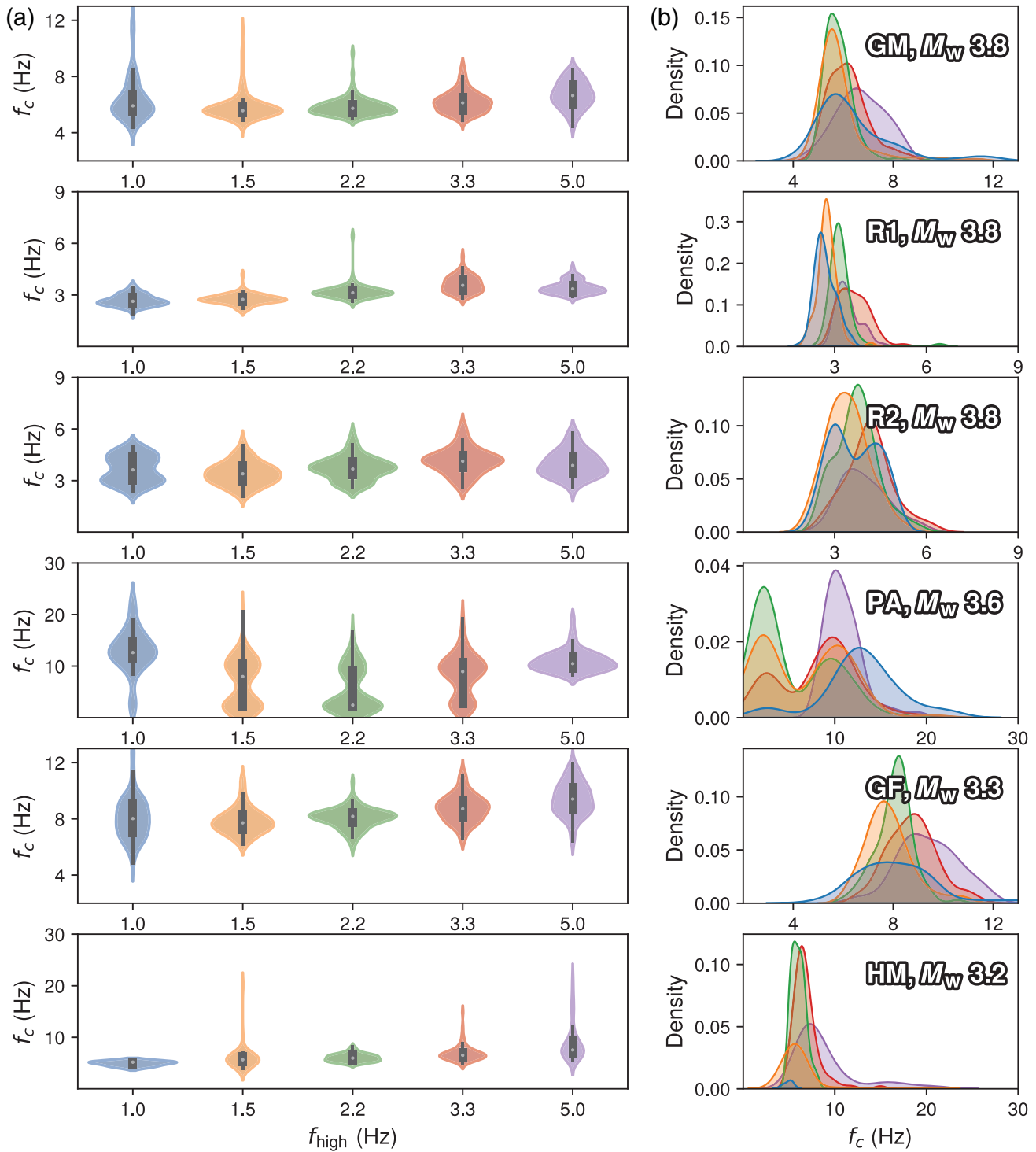


of the time window after P picks used in computing CC and deconvolution, shows no distinct trends with f_c estimate variations, except in PA (Fig. 6), presenting relatively consistent mode values for f_c estimates. However, detailed trends with increasing $nsec$ are event-specific, even for events of the same magnitude and in the same catalog, like R1 and R2.

The parameters defining the frequency bands (lower bound f_{low} and upper bound f_{high}) used in computing CC, affected the variations in the f_c estimates, as shown in Figures 7 and 8. An

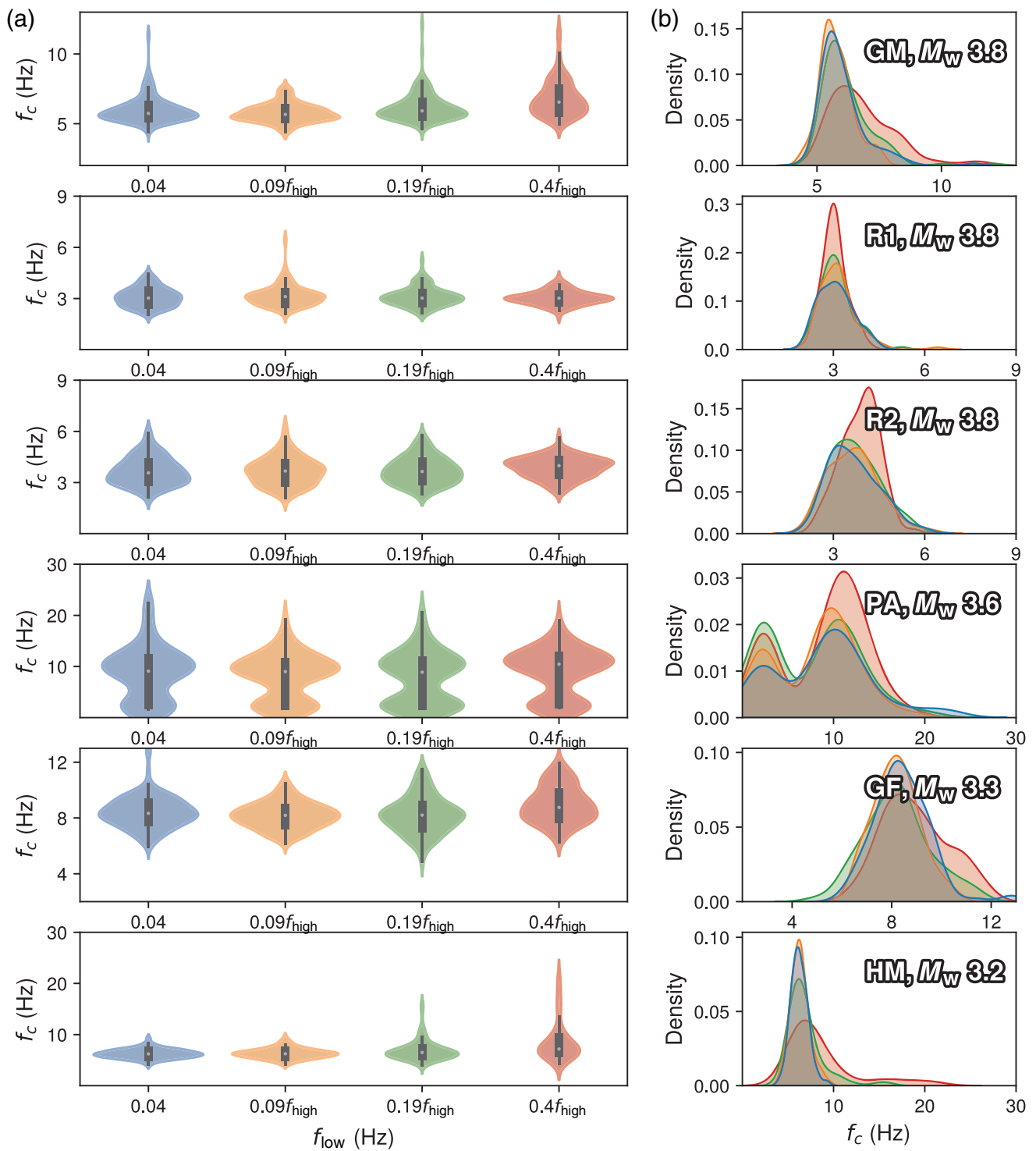
Figure 6. Variations in f_c estimates according to $nsec$, a length of time window after P picks: (a) violin plots (normalized distributions) for $nsec$ in set A as defined in Table 3; (b) plain distribution curves with the same details as those in panel (a).

f_{high} of 1 Hz yields diverse f_c estimation distributions (Fig. 7), especially for GM, GF, and HM, where f_c estimates tend to be higher than those of R1, R2, and PA (Fig. 3). Long-tailed f_c



estimate distributions are also visible at several f_{high} values (Fig. 7). Notably, the lowest f_c mode is at an f_{high} of 2.2 Hz, corresponding to the possible corner frequency in the first plateau of PA (Fig. 3d). Meanwhile, f_{low} does not significantly change the mode of f_c estimate distributions, except for f_{low} of $0.4 f_{\text{high}}$ (Fig. 8). The absolute value of f_{low} , not scaled from f_{high} , can also be checked in Figure S4, which presents higher f_{low} results in higher f_c .

Figure 7. Variations in f_c estimates according to f_{high} , the upper bound of frequency bands for band-pass filtering before computing CC between each EGF candidate and the target event: (a) violin plots (normalized distributions) for f_{high} in set A, as defined in Table 3, covering the range from 2.3 to 4.8 Hz, derived from Abercrombie *et al.* (2017) for earthquakes under low stress-drop conditions; (b) plain distribution curves with the same details as those in panel (a).



Highlighting low-frequency features

Varying frequency bands, window length, and CC criteria often caused the f_c estimates to display a single distribution with shifting mode values; in other cases, they were distinctly grouped. The higher f_c group corresponds to individual pulse durations, whereas the lower f_c group may reflect the event's overall duration, capturing its multiple structures. To capture lower frequency contents, we focused on which variable range (f_{low} , f_{high} , n_{sec} , CC_{cut}) highlighted the lower frequency parts without

Figure 8. Variations in f_c estimates according to f_{low} , the lower bound of frequency bands for band-pass filtering before computing CC between each EGF candidate and the target event: (a) violin plots (normalized distributions) for f_{low} in set A as defined in Table 3; (b) plain distribution curves with the same details as those in panel (a).

diverging or splitting the distribution. However, identifying the appropriate ranges focusing on low-frequency features was a qualitative task in this work, so we specified these ranges for

TABLE 4

Sets of the Selected Variable Ranges for the Target Earthquakes and Newly Defined Variables

ID	f_{low}^*	f_{high} (Hz)	$nsec$ (s)	CC_{cut}	Note
GM	0.09	1.5–2.2	2.1–5.1	0.8–0.9	Modified as set G
R1	0.04–0.40	1.0–2.2	2.1–5.1	0.6–0.7	Modified as set R
R2	0.04–0.19	1.0–1.5	2.1–2.7	0.6–0.7	Modified as set R
PA	0.04–0.19	1.5–3.3	3.3–5.1	0.8	Modified as set P
GF	0.04–0.09	2.2–5.0	2.1–5.1	0.9	Modified as set G
HM	0.04–0.09	1.5–3.3	2.1–5.1	0.8	Modified as set G
Set G	<0.05, 0.1, 4>	<1.8, 3.6, 5>	[2.1, 3.3, 0.3]	[0.7, 0.85, 0.05]	f_{min} of 0.9 Hz for HM
Set R	<0.04, 0.2, 4>	<1.2, 2.2, 5>	[2.4, 2.8, 0.1]	[0.6, 0.75, 0.05]	Using only two EGFs
Set P	<0.04, 0.2, 4>	<1.8, 3.0, 5>	[3.0, 4.2, 0.3]	[0.65, 0.8, 0.05]	–

f_{min} indicates the lower bound of frequency ranges for spectral fitting. The other notations are the same as in Table 3.

*The scaled f_{low} , anchored at an initial constant value of 0.04, as in Table 3.

each target event in Table 4. The spectral ratios, STFs, and f_c distributions in these ranges can be seen in Figure S5.

Based on the determined ranges, we redefined the variable sets as set G, set R, and set P in Table 4, following several guidelines described next. First, we preferred a shorter window length because a longer window generally results in a smaller CC and captures the onsets of S arrivals at close stations. Second, we did not use a CC_{cut} higher than 0.9 to prevent a decrease in the number of stations used, as higher CC values reduce the number of available stations (see Fig. 4, Fig. S3). This enabled us to observe the azimuthal distribution of f_c estimates. For the two target events, R1 and R2, we used only the two closest EGF events for each target because the EGF set selected solely based on CC values included events tens of kilometers away from the target event, as shown in Figure 4a. For the target event HM, we increased the lower bound of frequency ranges for spectral fitting from 0.8 to 0.9 Hz, due to instability in the first plateau below ~ 1 Hz, as shown in Figure 3f and Figure S5f. The spectral ratios, STFs, and f_c distributions estimated for R1, R2, and HM, without the adjustments described, are shown in Figure S6.

The redefined variable sets—set G for GM, GF, and HM; set R for R1 and R2; and set P for PA (Table 4)—initially had 400 combinations for f_{low} , f_{high} , $nsec$, and CC_{cut} . By counting only f_c estimates averaged from four or more stations, we obtained 400, 400, 397, 331, 400, and 309 deconvolution results for GM, R1, R2, PA, GF, and HM, respectively. These results yielded f_c estimate distributions that correspond well with both the spectral ratios and STFs (Fig. 9a–f). In particular, the STFs of event PA clearly show double peaks, with a major f_c estimate group matching the long-period structures (Fig. 9d). For event HM, the f_c estimates successfully captured only the long-period structure of the STFs (Fig. 9f).

DISCUSSION

Double peaks and rupture directivities

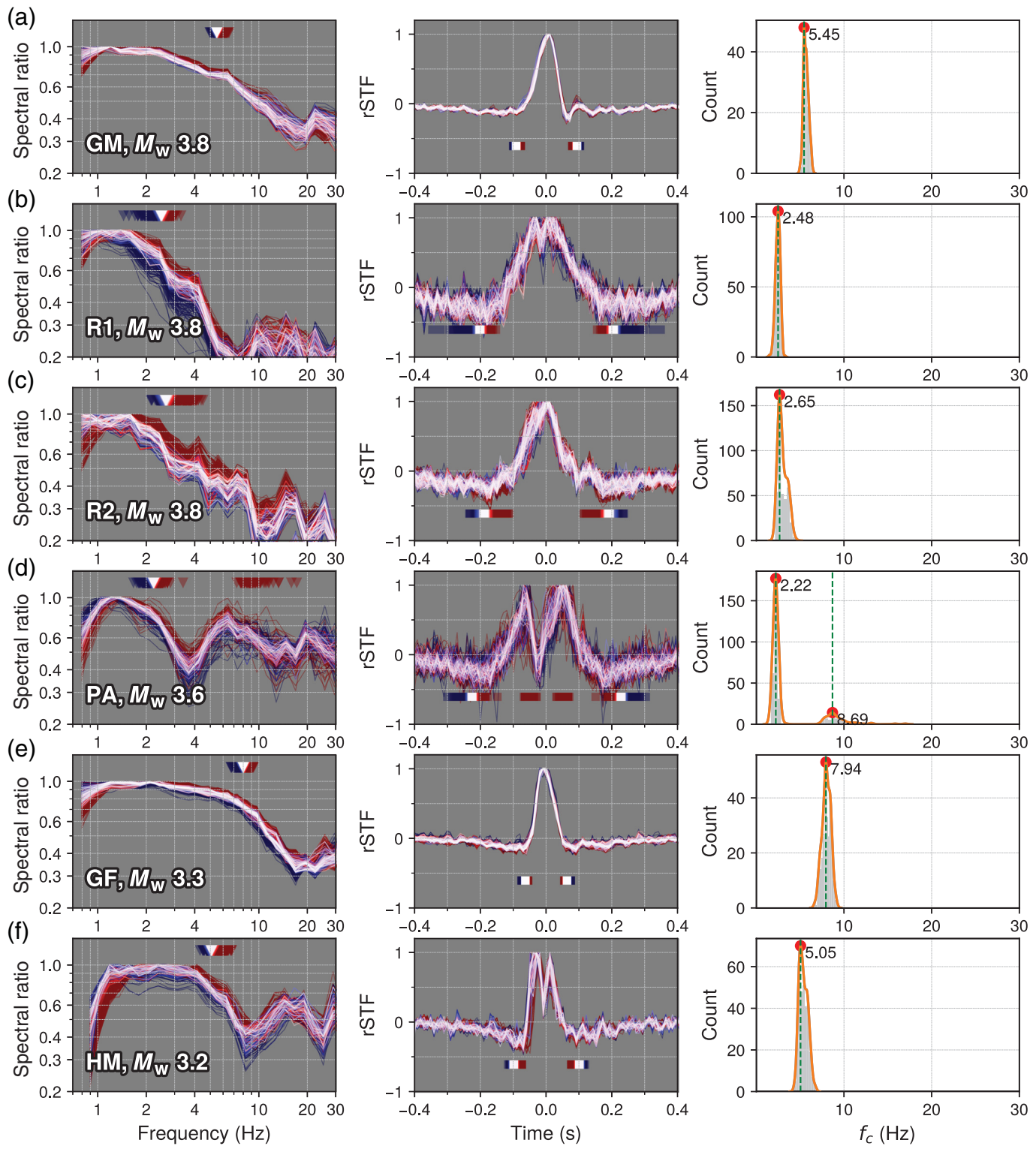
Are the observed multiple peaks for event PA and HM in STFs an artifact? Figure 10a,b shows repetitive double crests in the seismic record of the target events, PA and HM, which support

the presence of double peaks in the STFs derived for the two events. Figure 10c,d shows distinct double peaks corresponding to azimuthal variations in the rSTFs, averaged over 331 and 309 deconvolution results generated by set P for PA and set G for HM, respectively. This observation implies that events PA and HM did not rupture simply, such as a circular rupture. Meng *et al.* (2020) observed two clear pulses suggesting the existence of two major subevents for the M_w 4.6 event with clear variation in duration corresponding to the inferred rupture directivity. Oates *et al.* (2024) reported several unilateral ruptures displaying double to triple peaks in their rSTFs, attributed to azimuth-dependent Doppler broadening.

We analyzed rupture directivity by examining the reciprocals of f_c estimates (proportional to source durations) against azimuth (Fig. 11). The figure reveals notable variations in the distributions, particularly for events PA and HM, with the modes shifting with changes in azimuth. These azimuthal variations are also reflected in the results from the initial variable set, set A, as shown in Figure S7a. Specifically, for event PA, the paired $1/f_c$ values—resulting from the two distinct bumps in the spectral ratios observed in Figure 9d—are seen across all azimuths, as shown in the fourth row of Figure 11a and Figure S7a, suggesting azimuth-dependent changes in source duration. However, the significant azimuthal gap of PA toward the East Sea (Japan Sea) complicates pinpointing the rupture directivity. For HM, a possible unilateral pattern is suggested by the azimuthal changes in $1/f_c$ values (Fig. 11a) and azimuthal variations in the STF traces across stations (Fig. 10). No apparent dependence of $1/f_c$ on hypocentral distance was observed, as shown in Figure 11b and Figure S7b.

f_c estimate uncertainty variation

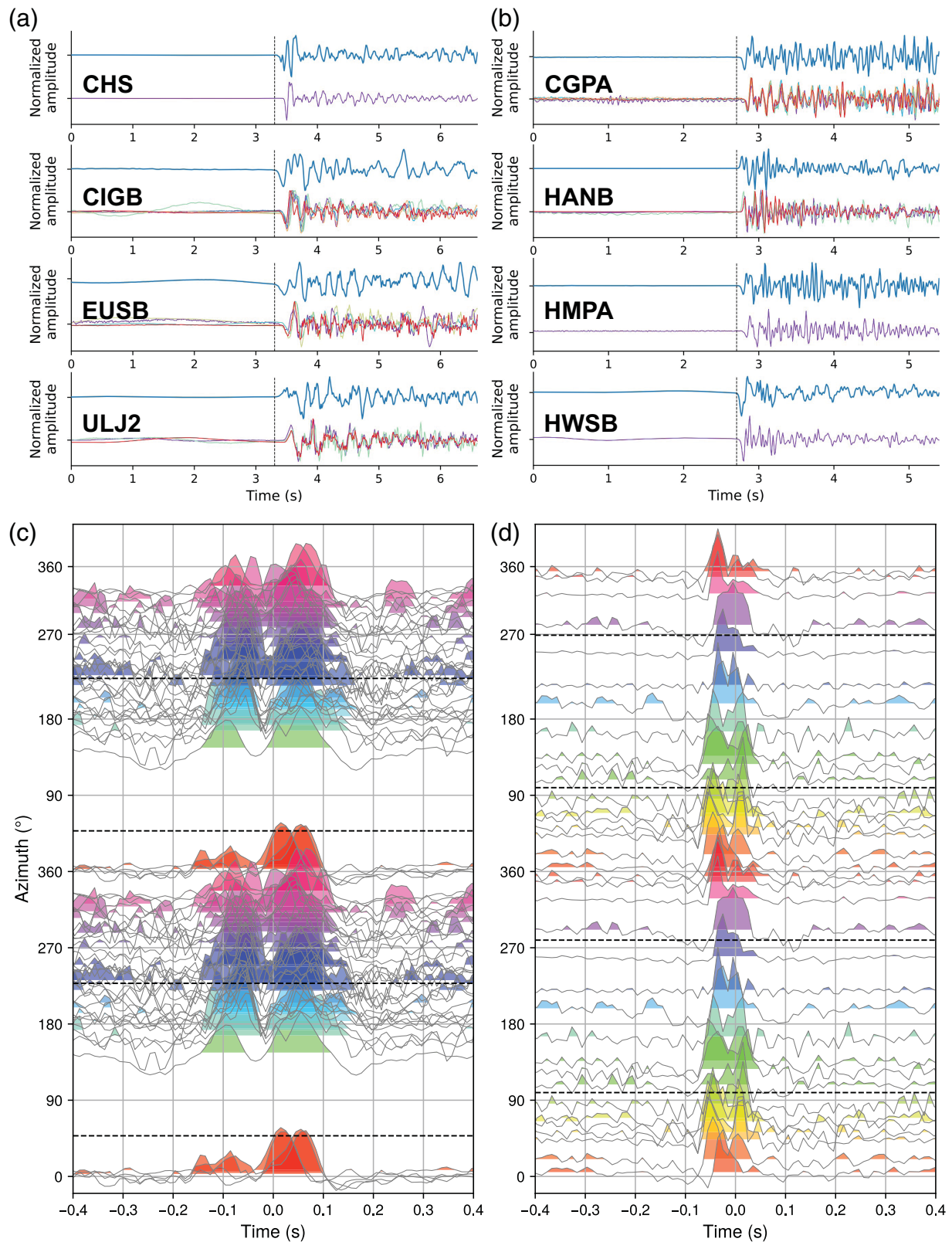
The reciprocals of f_c estimates, particularly for PA, often fail to capture the overall duration of the STF, as shown in Figures 3 and 9. We compared the f_c estimates to the time T , defined as the interval between the onset and offset of the STFs (Fig. 12). The onset and offset were detected after smoothing the signal using a moving window average (i.e., convolution with a time



window of unit area). In Figure 12a, for each moving window length (denoted by colors), the reciprocal of T shows significantly less variation compared to the f_c estimates. In Figure 12b, T captures the overall features of the rSTFs, as we set a minimum signal duration during the onset-offset detection. Discrepancies among the groups of T reciprocals are around several Hertz, similar to the variation levels observed in the f_c estimates. However, it was challenging to define the slopes

Figure 9. Normalized spectral ratios, rSTFs, not filtered, and f_c estimate distributions for (a) GM; (b) PA; (c) R1; (d) R2; (e) GF; and (f) HM, generated by iterations of the workflow in Figure 2 with each set defined in Table 4. Details are the same as those in Figure 2.

between the f_c estimates and the reciprocals of T , which are associated with the high-frequency fall-off of the spectrum (f_c see dashed lines in Figure 12a, representing slopes of 1, $\pi/2$,



and π). Because we applied a simple onset–offset detection method, using a more advanced technique, such as the projected Landweber deconvolution algorithm (Meng *et al.*, 2020; Han *et al.*, 2024), could lead to more accurate source duration measurements and support further comparisons between source durations and f_c values estimated from spectral fitting.

Figure 10. Seismograms with double peaks for (a) PA and (b) HM, showing the target signal (upper) and the EGF (lower) in each panel. Azimuthal variations in unfiltered STFs for (c) PA and (d) HM. The stacked deconvolution results were generated using each variable set (f_{low} , f_{high} , n_{sec} , and CC_{cut}) from a total of 400 sets defined in set P for PA and set G for HM.

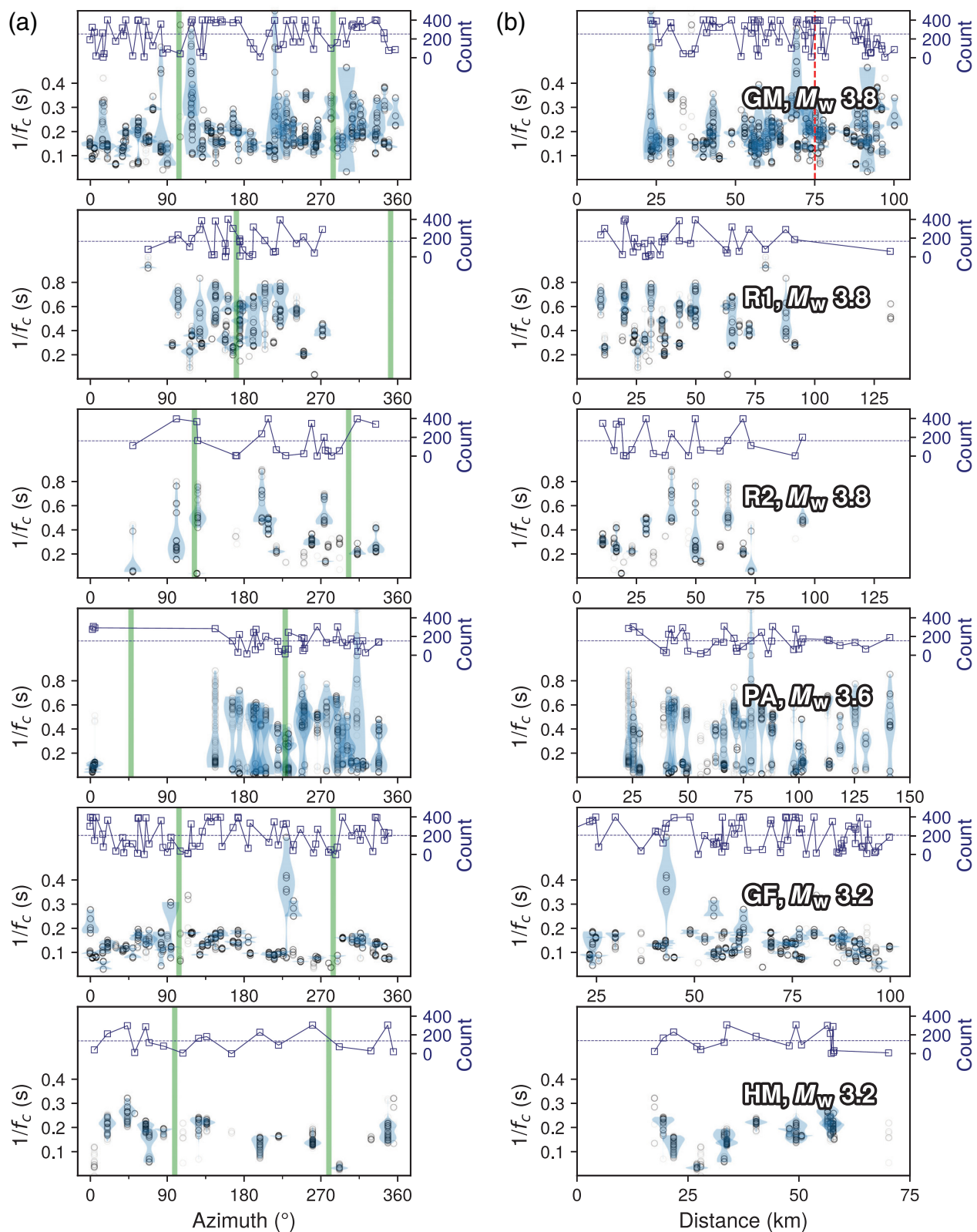


Figure 11. Variations in $1/f_c$ estimates for the six target events at each station, ordered by (a) azimuth and (b) hypocentral distances from the target. The count represents the number of times a station is used across varying $nsec$, f_{low} , f_{high} , and CC_{cut} . The green vertical lines indicate a strike and its opposite end (i.e., $+180^\circ$) when assuming a lineament based on the references for each earthquake in Table 1. A red dashed line in the first row of panel (b) indicates the distance where an S wavetrain of GF started proceeding with a P wavetrain of GM.

and its opposite end (i.e., $+180^\circ$) when assuming a lineament based on the references for each earthquake in Table 1. A red dashed line in the first row of panel (b) indicates the distance where an S wavetrain of GF started proceeding with a P wavetrain of GM.

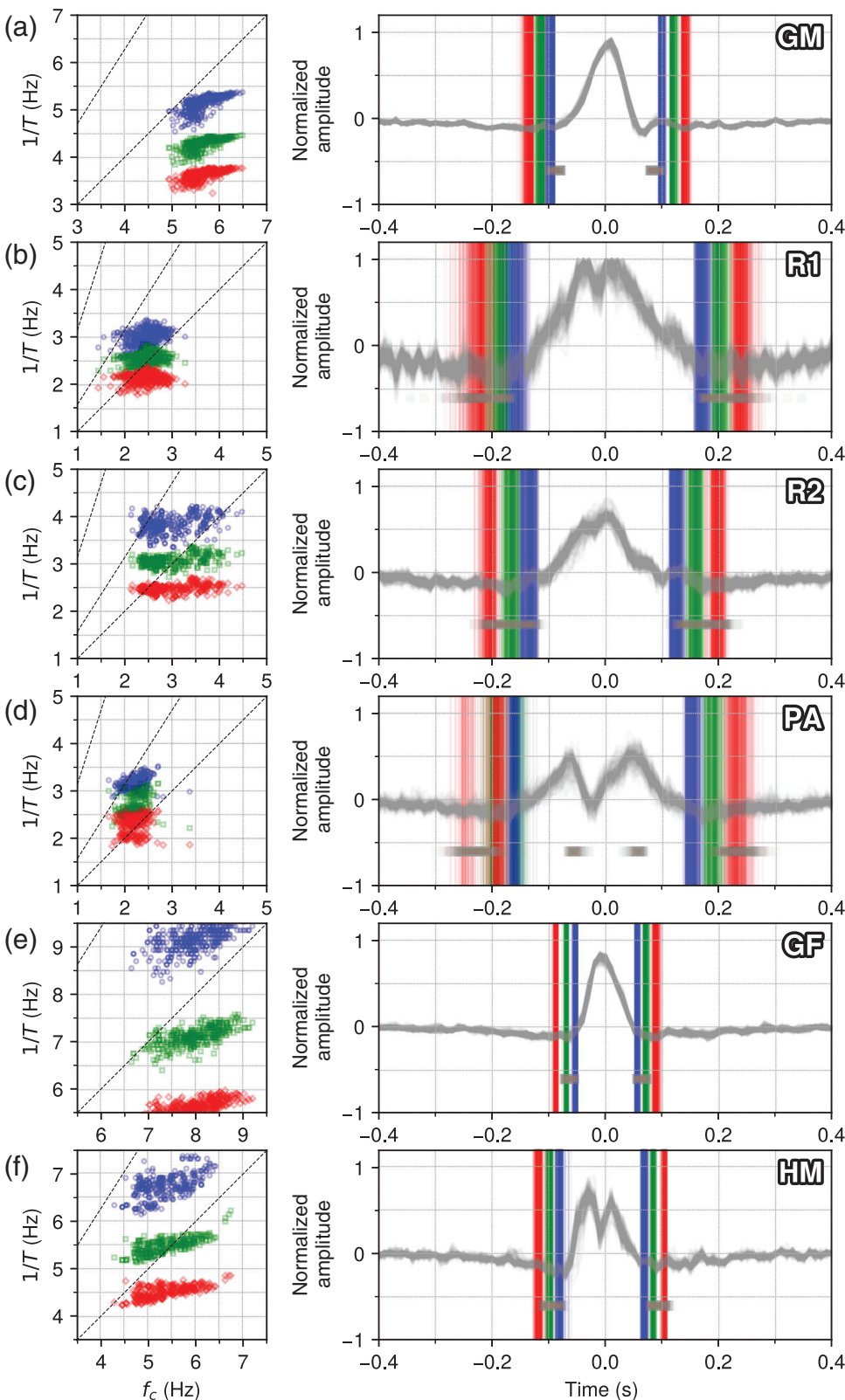


Figure 12. Comparisons of f_c estimates from curve-fitting spectral ratios with durations determined from rSTFs for six target events, (a) GM; (b) R1; (c) R2; (d) PA; (e) GF; and (f) HM. The left column shows the relationship between f_c estimates and $1/T$, where T represents the duration of the rSTF, determined by the difference between the onset and offset. The right column displays the normalized rSTF for each event, with the corresponding onset and offset times identified using a smoothed signal and a noise threshold, with varying smoothing levels for each target. Onset/offset pairs are color-coded based on the smoothing level.

Instead, we focus on the uncertainty of f_c estimates derived from the curve fitting the spectral ratios. First, we present the standard errors, σ_{err} , for individual results of the six target events, as shown in Table 5 and Figure 13. The standard error for each result was derived from the estimated covariance matrix during the curve-fitting procedures, using one specific combination of f_{low} , f_{high} , $nsec$, and CC_{cut} from the refined variable set corresponding to each target event. Figures S8–S13 specify the values for f_{low} , f_{high} , $nsec$, and CC_{cut} in the figure captions. These individual results for the six target events were selected through visual inspection, prioritizing those with low f_c values close to the mode of f_c estimates and those displaying consistent directivity patterns across all variable sets, as seen in Figure 11a.

The standard errors for each selected result are comparable to the standard deviations of f_c estimates from the refined variable set for each target event (Table 5, Fig. 13), except for set P in event PA, which shows higher f_c groups. It is important to note that the standard error for each result does not reflect the discrepancies from other f_c estimates reported in previous studies for each target event (Table 5, Fig. 13). In contrast, the standard deviations of f_c estimates from set A—a comprehensive range set for f_{low} , f_{high} , $nsec$, and CC_{cut} —account for the discrepancies observed in previous studies. This suggests that the f_c distributions generated by set A capture potential variations in f_c estimates for the six target events, derived

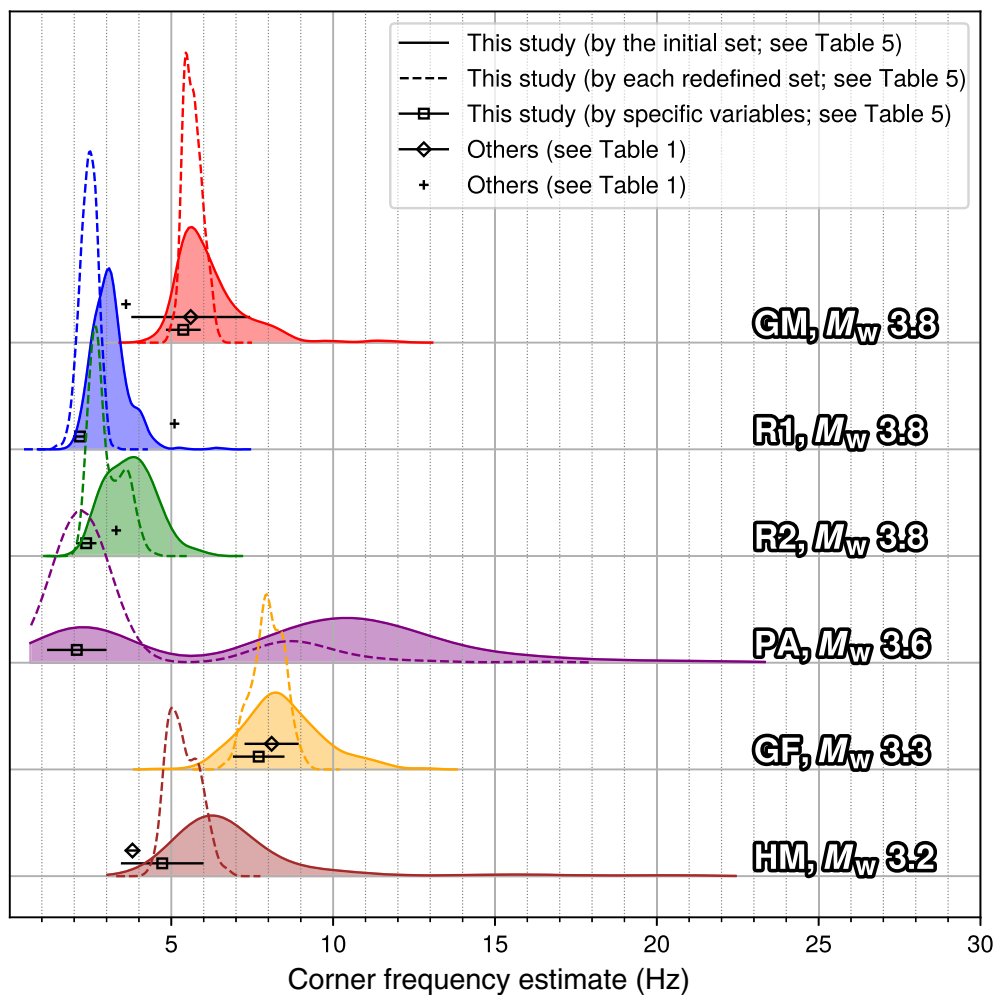


Figure 13. Variations in f_c estimates according to differences in methods. The estimation approaches used in the results labeled as “Others” differ as specified in Table 1; whereas the details of the EGF approaches employed in this study are provided in Table 5. The color version of this figure is available only in the electronic edition.

through different methods, underscoring the limitations of relying solely on the standard error to represent estimation uncertainty.

Other considerations in f_c estimation

We presented how f_c estimates vary with EGF selection based on CC. However, even when the same spectral ratio is obtained,

the choice of frequency range for curve fitting can affect f_c estimates. For example, for the HM event with the redefined variable set, set G, we increased the lower bound of the frequency range for spectral fitting, f_{\min} , from 0.8 to 0.9 (Table 4, Fig. 9f), which resulted in lower f_c estimates compared to when f_{\min} was 0.8 (Fig. 13). As shown in Figure 14, increasing f_{\min} causes the mode of f_c estimates to decrease. This occurred because f_{\min} was defined to be lower than the flat part of the first plateau in the observed spectral ratios, leading to an underdetermined long-period level.

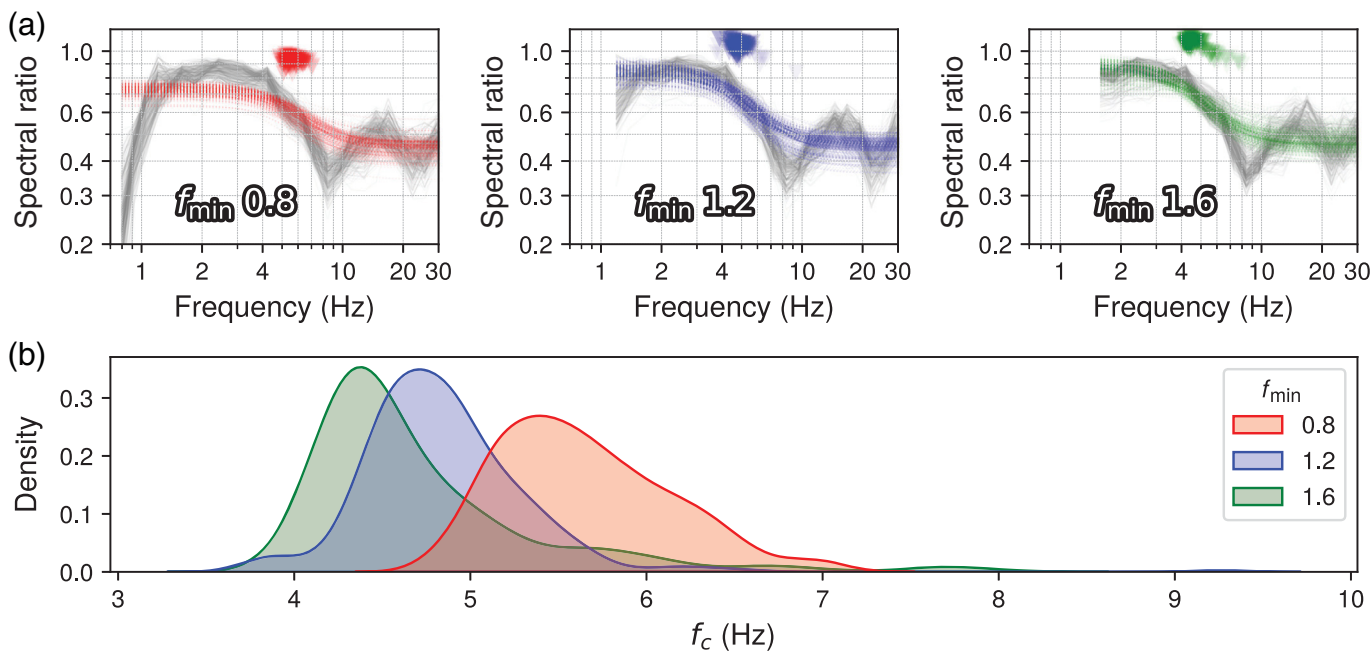
As another factor, signal quality, specifically the signal-to-noise ratio (SNR), was not explicitly considered in our analysis. We assumed that events identified as EGFs using the CC criterion would have sufficient signal amplitudes due to their waveform similarity to the target event, which typically implies high SNR. This assumption proved valid in most cases, as demonstrated in Figure S14, where the linear SNR of selected events pre-

dominantly exceeded 3. Nevertheless, because high CC values do not always guarantee high SNR, we applied a linear $\text{SNR} > 3$ constraint and observed minimal impact on the shapes of spectral ratios and STFs (Fig. S15) or the distributions of f_c estimates (Fig. S16).

Higher frequency bands, similar to those used for relocation purposes (e.g., Son *et al.*, 2018; Trugman *et al.*, 2020), were also

TABLE 5
Standard Deviations in f_c Estimates by Variable Sets

Target / (Hz)	GM	R1	R2	PA	GF	HM	Note
$f_{c,\text{Mode}}$	5.48	3.09	3.79	2.3	8.27	6.28	Using the initial (wide ranging) variable set, set A, in Table 3
Std.	1.08	0.54	0.76	4.75	1.22	2.53	
$f_{c,\text{Mode}}$	5.45	2.48	2.65	2.22	7.94	5.05	Using the redefined variable sets in Table 4 (set G, set R, and set P)
Std.	0.29	0.27	0.49	2.86	0.49	0.48	
f_c	5.37	2.18	2.37	2.08	7.70	4.72	Using specific variables from the redefined sets (detailed in Figs. S8–S13 captions)
Error	0.25	0.09	0.14	0.44	0.38	0.62	



tested for computing CC during EGF selection (Fig. S17). These bands did not change the shapes of spectral ratios or STFs for GM and GF, which exhibited relatively high f_c estimates. However, for R1 and R2, the number of valid results obtained from four or more stations was too small. For PA and HM, the averaged STFs missed the double-peak feature due to differences in the alignment of the long-period structure (Fig. S18).

Setting a minimum value for the magnitude difference between the target and EGF candidates is another adjustable factor in EGF selection. Using the set A, we increased this threshold from 0.4 to 0.6 and 1.0. Although this adjustment reduced the level of the second plateau in the spectral ratio, the overall characteristics of the spectral ratios and STFs remained unchanged, except for the complex PA event (Fig. S19).

Beyond f_c uncertainty: k and β in earthquake stress drop

We displayed stress-drop variations with varying f_c within $\pm 2\sigma$ for the six target events, as shown in Figure 15. Figure 15a uses f_c estimates from individual results with σ_{err} from curve fitting, whereas Figure S20a,b shows the f_c mode with standard deviations from the refined and initial variable sets, respectively. As we move from Figures 15a to S20, the increasing standard deviations in f_c estimate distributions make it more difficult to discern differences in stress-drop estimates between target events, due to the growing variability in stress-drop estimates for each event. This trend highlights the limitations of systematic earthquake stress-drop estimations, as the f_c variations using set A likely represent discrepancies in f_c estimates derived through different methods, suggesting the need for caution when focusing on individual estimate values.

Figure 14. Variations in f_c estimates for HM with changes in the lower bound of the frequency range used for curve fitting (f_{\min}) from 0.8 to 1.2 and 1.6: (a) observed and modeled spectral ratios, along with f_c estimates generated by iterations of the workflow in Figure 2 with set G in Table 4 for each f_{\min} value; (b) distributions of f_c estimates for each f_{\min} value.

The other notable aspect is that for at least two of the six target events, PM and HM, the assumption of a circular rupture may not hold, raising questions about the accuracy of stress-drop calculations that use a value for k derived from this assumption. The k -value for S waves can vary even within the same Brune's circular crack model (Brune, 1970, 1971) depending on S , a correction factor for converting S waves to P waves. For example, k is 0.360 at $S = 0.7$, 0.372 at $S = 0.8$, and 0.384 at $S = 0.9$. An increase in k leads to a decrease in rupture radius, which consequently reduces the stress drop significantly, as indicated by the cubic relationship in equations (1) and (2). Furthermore, the shear-wave velocity term, β , in equation (2), which is assumed to be proportional to the rupture velocity, exacerbates the uncertainties in stress-drop estimates (Zhang et al., 2022). To address these uncertainties, some studies, such as Trugman (2020), have utilized a local velocity model. Abercrombie (2021) explored variations in stress-drop estimates related to the increase in shear velocity with depth, suggesting that focal depth is one of the factors impacting stress-drop estimation. Ji and Archuleta (2021), using their double-corner-frequency model, suggest that either stress drop or rupture velocity is magnitude-dependent. However, the six target events have a narrow range in magnitude differences (M_w 3.2–3.8), which allows us to minimize magnitude-dependent characteristics when examining variations in stress-drop estimates.

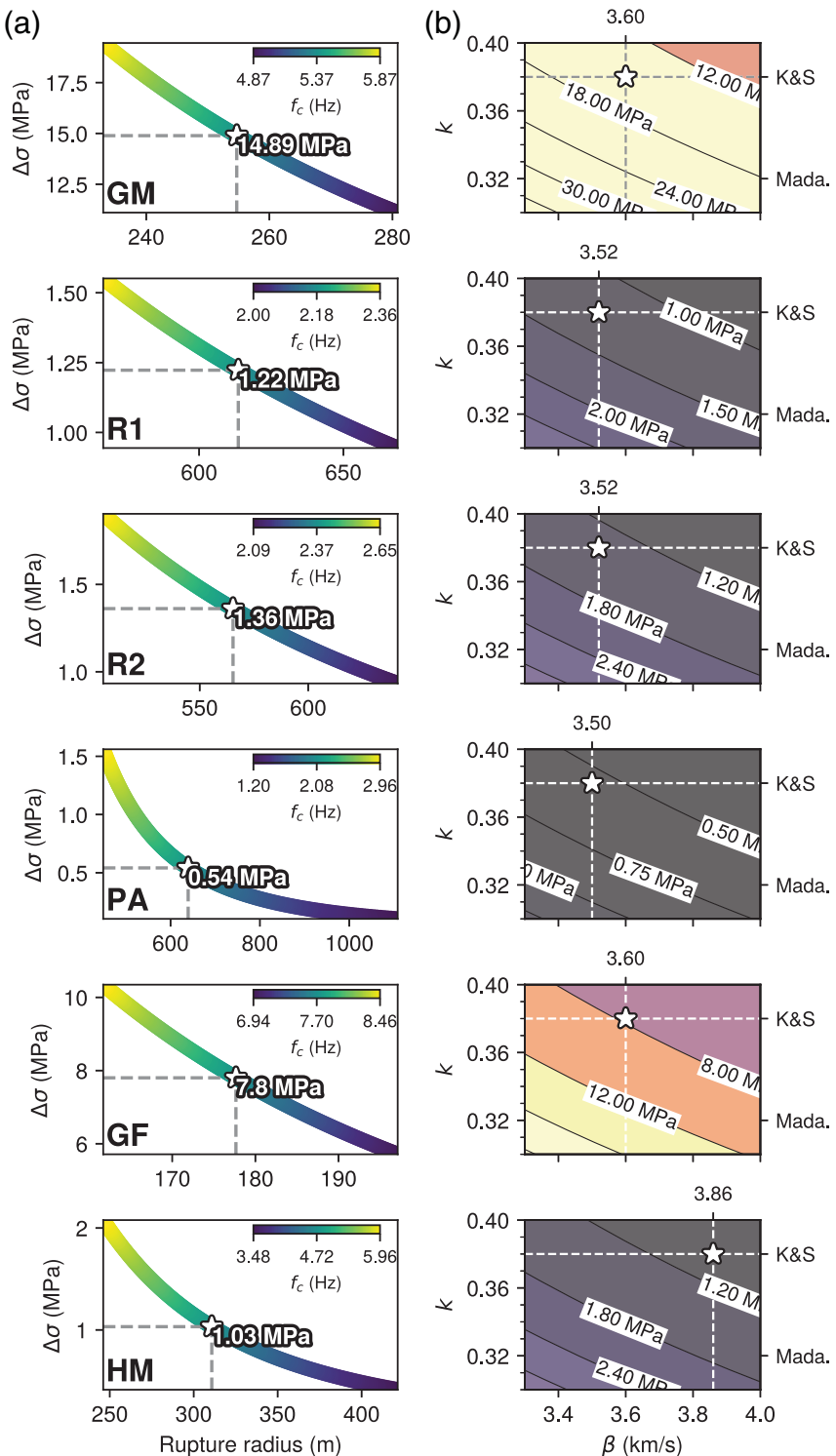


Figure 15. Stress-drop variation example: (a) according to the f_c estimates varying by $\pm 2\sigma$ with a fixed k of 0.38 at the assumed shear velocity β ; (b) according to a rupture characteristic of k and an assumed β , with a fixed f_c for each target event. The stars indicate stress-drop estimates, the values for them are labeled in panel (a). The assumed β for each event is indicated by dashed line in panel (b), cited from each corresponding reference (listed in Table 1). “K&S” and “Mada.” in panel (b) indicate k for P waves from Kaneko and Shearer (2014) and Madariaga (1976), respectively, when a rupture velocity of β is assumed to be 0.9. The standard deviation, σ , is for the fixed f_c estimate in panel (b), computed from the procedure for spectral ratio fitting (listed in Table 5). The specific variable set used for each event can be found in Figures S8–S13, which present detailed results for each event, including the recovered rSTFs and observed modeled spectral ratios at every station.

We investigated the variability of stress drops in response to changes in k and β for the six target events, utilizing fixed values for f_c estimates, derived from the individual example results depicted in Figures S8–S13. For estimating M_0 , we used independently estimated M_w values (listed in Table 1) instead of computing M_0 ratios between each EGF and target. The calculated stress drop varies by about two to three times across the six target events (Fig. 15b), and this variability becomes significant as f_c increases due to the cubic relationship between f_c and $\Delta\sigma$. However, despite this variability, the stress drops for the two earthquakes, GM and GF, which occurred in the central Korean Peninsula, known for their low seismicity rate, are relatively larger than those of other events.

In contrast, the stress-drop estimates for events PA and HM exhibit relatively lower values, comparable to those of events R1 and R2, which occurred in the Ridgecrest area, California, though the f_c computed for PA shows one of the largest uncertainties (Table 5). Son *et al.* (2020) reported the migration of earthquake clusters in the 2017 Pohang earthquake sequence (this sequence includes event PA, though migration does not), matching a fluid diffusion curve during the first 18 hr. Similarly, Son *et al.* (2021) reported hypocenter migration also matching a fluid diffusion curve during the 14 days of the 2020 Haenam earthquake sequence, which includes event HM. Although some studies relate low stress drops to

fluid-fault interactions and seismicity migration (e.g., Hatch *et al.*, 2020), the stress-drop estimates from only two events (PA and HM) are very limited for discussing the migratory behavior of earthquakes.

CONCLUSION

This study examined the uncertainties and variations in corner-frequency (f_c) estimates and their impact on stress-drop ($\Delta\sigma$) estimates for six earthquakes with magnitudes between M_w 3.2 and 3.8 from the Ridgecrest sequence in California (events R1 and R2) and the Korean Peninsula (events GM, GF, PA, and HM). By focusing on earthquakes with similar magnitudes, we aimed to minimize the influence of magnitude differences and provide a more controlled comparison of f_c and $\Delta\sigma$ estimates across diverse seismicity patterns in different tectonic settings. Utilizing high-definition seismic catalogs already created for the earthquake sequences studied, we applied the EGF approach along with a systematic workflow for deconvolution and spectral fitting. We assessed the variability in corner frequency based solely on CCs, regardless of magnitude differences between each potential EGF and the target event, and without considering whether the potential EGFs were foreshocks or aftershocks. This approach allowed us to investigate the effects of varying frequency bands and window lengths in computing CC and CC criteria in EGF selection.

The study found variations in spectral shapes and STFs across the six target events, reflecting diverse source characteristics and complexities. Specifically, events R1, R2, and GM, despite having the same magnitude (M_w 3.8), exhibit distinct f_c estimate distributions, suggesting that earthquake source characteristics and the corresponding variations in source parameters, including f_c , are dependent on the style of faulting and the mechanical properties along the fault where each event was generated. For event PA, the assumption of a circular rupture did not hold, as indicated by its spectral ratios and STFs, which presented one of the lowest f_c estimates. Event HM displayed rupture directivity, along with its intricate STFs featuring clear double peaks. Stress-drop estimates for GM and GF were relatively high compared to other regions, whereas PA and HM exhibited lower stress drops similar to the Ridgecrest events. These findings persisted despite variations in f_c estimates and changes in rupture characteristic constants (k and β).

However, achieving consistency, as observed in the persistence of $\Delta\sigma$ estimate discrepancies among the target events, was challenging due to a group of higher f_c estimates. These higher f_c estimates usually resulted from variations in the CC criterion for EGF selections and the upper bound of the frequency band used in computing CC. The mode and shape of f_c estimate distributions were significantly influenced by the variable sets, leading to the formation of higher f_c groups and sometimes splitting the f_c distributions into higher and lower

f_c groups. The higher f_c group, with its cubic-scale error propagation, obscures $\Delta\sigma$ differences among events, increasing the uncertainty of $\Delta\sigma$ estimates for an individual event. This highlights the limitations of systematic f_c estimations, especially when dealing with source complexity and tectonic diversity. Although detailed adjustments of the variables to focus on low-frequency features addressed the issue for the events studied here, we suggest caution when interpreting individual f_c and $\Delta\sigma$ estimates.

DATA AND RESOURCES

A part of the continuous waveform data used in this study can be accessed at <https://data.kigam.re.kr/quake/> and <https://necis.kma.go.kr/> following approval. These resources are operated by the Korea Institute of Geoscience and Mineral Resources (KIGAM) and the Korea Meteorological Administration (KMA). In addition, a catalog and waveform data for the 55 events in 2019 Ridgecrest earthquake sequence, available for the Southern California Earthquake Center (SCEC)/U.S. Geological Survey (USGS) Community Stress Drop Validation Study, can be found at <https://scedc.caltech.edu/data/stressdrop-ridgecrest.html> organized by Trugman (2020). The authors used Inkscape (<https://inkscape.org/>). All websites were last accessed in February 2025. The supplemental material for this article includes Text S1, Tables S1 and S2, and Figures S1–S20, citing Mogi (1963), Zaliapin and Ben-Zion (2013a, b), Goebel *et al.* (2019), Son *et al.* (2020, 2021), and Lim *et al.* (2024).

DECLARATION OF COMPETING INTERESTS

The authors acknowledge that there are no conflicts of interest recorded.

ACKNOWLEDGMENTS

The authors appreciate the thoughtful insights provided by the editor, R. E. Abercrombie, and two anonymous reviewers, who contributed significantly to this study. The authors also acknowledge C. S. Cho, S. G. Song, H. Lim, S. -Y. Baag, W.-Y. Kim, and M.-S. Seo for the discussion regarding source parameters. The authors thank the Korea Meteorological Administration and the Korea Institute of Nuclear Safety for providing the seismic data used in this study. In addition, the authors express their gratitude to the authors of Generic Mapping Tools (Wessel *et al.*, 2019), Matplotlib (Hunter, 2007), and Seaborn (Waskom, 2021). This study was supported by the Basic Research Project of KIGAM funded by the Ministry of Science and ICT (MSIT, Republic of Korea).

REFERENCES

- Abercrombie, R. E. (2014). Stress drops of repeating earthquakes on the San Andreas Fault at Parkfield, *Geophys. Res. Lett.* **41**, no. 24, 8784–8791, doi: [10.1002/2014GL062079](https://doi.org/10.1002/2014GL062079).
- Abercrombie, R. E. (2021). Resolution and uncertainties in estimates of earthquake stress drop and energy release, *Phil. Trans. Roy. Soc. Lond. A* **379**, no. 2196, 20200131, doi: [10.1098/rsta.2020.0131](https://doi.org/10.1098/rsta.2020.0131).
- Abercrombie, R. E., S. Bannister, J. Ristau, and D. Doser (2017). Variability of earthquake stress drop in a subduction setting, the Hikurangi Margin, New Zealand, *Geophys. J. Int.* **208**, no. 1, 306–320, doi: [10.1093/gji/ggw393](https://doi.org/10.1093/gji/ggw393).

- Aki, K. (1967). Scaling law of seismic spectrum, *J. Geophys. Res.* **72**, no. 4, 1217–1231, doi: [10.1029/JZ072i004p01217](https://doi.org/10.1029/JZ072i004p01217).
- Baltay, A., R. E. Abercrombie, S. Chu, and T. Taira (2024). The SCEC/USGS community stress drop validation study using the 2019 Ridgecrest earthquake sequence, *Seismica* **3**, no. 1, doi: [10.26443/seismica.v3i1.1009](https://doi.org/10.26443/seismica.v3i1.1009).
- Boatwright, J. (1978). Detailed spectral analysis of two small New York state earthquakes, *Bull. Seismol. Soc. Am.* **68**, no. 4, 1117–1131.
- Brune, J. N. (1970). Tectonic stress and the spectra of seismic shear waves from earthquakes, *J. Geophys. Res.* **75**, no. 26, 4997–5009, doi: [10.1029/JB075i026p04997](https://doi.org/10.1029/JB075i026p04997).
- Brune, J. N. (1971). Correction [to “Tectonic stress and the spectra of seismic shear waves from earthquakes”], *J. Geophys. Res.* **76**, no. 20, 4711–5002, doi: [10.1029/JB076i020p05002](https://doi.org/10.1029/JB076i020p05002).
- Calderoni, G., and R. E. Abercrombie (2023). Investigating spectral estimates of stress drop for small to moderate earthquakes with heterogeneous slip distribution: Examples from the 2016–2017 Amatrice earthquake sequence, *J. Geophys. Res.* **128**, no. 6, e2022JB025022, doi: [10.1029/2022JB025022](https://doi.org/10.1029/2022JB025022).
- Chaves, E. J., S. Y. Schwartz, and R. E. Abercrombie (2020). Repeating earthquakes record fault weakening and healing in areas of mega-thrust postseismic slip, *Sci. Adv.* **6**, no. 32, eaaz9317, doi: [10.1126/sciadv.aaz9317](https://doi.org/10.1126/sciadv.aaz9317).
- Dreger, D. (2003). TDMT_INV: Time domain seismic moment tensor inversion, *Int. Geophys.* **81**, 1627–1628.
- Goebel, T. H. W., Z. Rosson, E. E. Brodsky, and J. I. Walter (2019). Aftershock deficiency of induced earthquake sequences during rapid mitigation efforts in Oklahoma, *Earth Planet. Sci. Lett.* **522**, 135–143, doi: [10.1016/j.epsl.2019.06.036](https://doi.org/10.1016/j.epsl.2019.06.036).
- Han, S., W.-Y. Kim, J. Y. Park, M.-S. Seo, and Y.-H. Kim (2024). Rupture model of the 5 April 2024 Tewksbury, New Jersey, earthquake based on regional L-g wave data, *Seism. Rec.* **4**, no. 3, 214–222, doi: [10.1785/0320240020](https://doi.org/10.1785/0320240020).
- Hatch, R. L., R. E. Abercrombie, C. J. Ruhl, and K. D. Smith (2020). Evidence of aseismic and fluid-driven processes in a small complex seismic swarm near Virginia City, Nevada, *Geophys. Res. Lett.* **47**, no. 4, e2019GL085477, doi: [10.1029/2019GL085477](https://doi.org/10.1029/2019GL085477).
- Hunter, J. D. (2007). Matplotlib: A 2D graphics environment, *Comput. Sci. Eng.* **9**, no. 3, 90–95, doi: [10.1109/MCSE.2007.55](https://doi.org/10.1109/MCSE.2007.55).
- Ji, C., and R. J. Archuleta (2021). Two empirical double-corner-frequency source spectra and their physical implications, *Bull. Seismol. Soc. Am.* **111**, no. 2, 737–761, doi: [10.1785/0120200238](https://doi.org/10.1785/0120200238).
- Kaneko, Y., and P. M. Shearer (2014). Seismic source spectra and estimated stress drop derived from cohesive-zone models of circular subshear rupture, *Geophys. J. Int.* **197**, no. 2, 1002–1015, doi: [10.1093/gji/ggu030](https://doi.org/10.1093/gji/ggu030).
- Kim, W. -Y., M. -S. Seo, J. Y. Park, S. Han, Y. O. Son, and Y. Kim (2023). The 28 October 2022 3.8 Goesan earthquake sequence in central Korea: Stress drop, aftershock triggering, and fault interaction, *Bull. Seismol. Soc. Am.* **113**, no. 6, 2416–2431. doi: [10.1785/0120230078](https://doi.org/10.1785/0120230078).
- Krischer, L., T. Megies, R. Barsch, M. Beyreuther, T. Lecocq, C. Caudron, and J. Wassermann (2015). ObsPy: A bridge for seismology into the scientific Python ecosystem, *Comput. Sci. Discov.* **8**, no. 1, 014003, doi: [10.1088/1749-4699/8/1/014003](https://doi.org/10.1088/1749-4699/8/1/014003).
- Lim, H., C. S. Cho, and M. Son (2024). The 2022 Goesan earthquake of the moment magnitude 3.8 along the buried fault in the central Korean Peninsula, *J. Seismol.* **28**, 519–534, doi: [10.1007/s10950-024-10201-y](https://doi.org/10.1007/s10950-024-10201-y).
- Madariaga, R. (1976). Dynamics of an expanding circular fault, *Bull. Seismol. Soc. Am.* **66**, no. 3, 639–666, doi: [10.1785/BSSA0660030639](https://doi.org/10.1785/BSSA0660030639).
- Mayeda, K., and W. R. Walter (1996). Moment, energy, stress drop, and source spectra of western United States earthquakes from regional coda envelopes, *J. Geophys. Res.* **101**, no. B5, 11195–11208, doi: [10.1029/96JB00112](https://doi.org/10.1029/96JB00112).
- Meng, H., J. J. McGuire, and Y. Ben-Zion (2020). Semiautomated estimates of directivity and related source properties of small to moderate Southern California earthquakes using second seismic moments, *J. Geophys. Res.* **125**, e2019JB018566, doi: [10.1029/2019JB018566](https://doi.org/10.1029/2019JB018566).
- Mogi, K. (1963). Some discussions on aftershocks, foreshocks and earthquake swarms: the fracture of a semi-infinite body caused by an inner stress origin and its relation the earthquake phenomena, *Bull. Earthq. Res. Inst.* **4**, no. 3, 615–658, doi: [10.15083/0000033716](https://doi.org/10.15083/0000033716).
- Morasca, P., D. Bindi, K. Mayeda, J. Roman-Nieves, J. Bsarno, W. R. Walter, and D. Spallarossa (2022). Source scaling comparison and validation in Central Italy: data intensive direct S waves versus the sparse data coda envelope methodology, *Geophys. J. Int.* **231**, no. 3, 1573–1590, doi: [10.1093/gji/gjac268](https://doi.org/10.1093/gji/gjac268).
- Newville, M., R. Otten, A. Nelson, T. Stensitzki, A. Ingargiola, D. Allan, A. Fox, F. Carter, R. Osborn, D. Pustakhod, et al. (2022). lmfit/lmfit-py: 1.1.0 (1.1.0), *Zenodo*, doi: [10.5281/zenodo.7370358](https://doi.org/10.5281/zenodo.7370358).
- Oates, S., J. Schmitz, B. Zurek, T. Piesold, and E. van Dedem (2024). Empirical Green’s function analysis of some induced earthquake pairs from the Groningen gas field, *J. Seismol.* doi: [10.1007/s10950-024-10204-9](https://doi.org/10.1007/s10950-024-10204-9).
- Prieto, G. A. (2022). The multitaper spectrum analysis package in Python, *Seismol. Res. Lett.* **93**, no. 3, 1922–1929, doi: [10.1785/0220210332](https://doi.org/10.1785/0220210332).
- Ruhl, C. J., R. E. Abercrombie, and K. D. Smith (2017). Spatiotemporal variation of stress drop during the 2008 Mogul, Nevada, earthquake swarm, *J. Geophys. Res.* **122**, no. 10, 8163–8180, doi: [10.1002/2017JB014601](https://doi.org/10.1002/2017JB014601).
- Schaff, D. P., G. H. R. Bokelmann, W. L. Ellsworth, E. Zanzerkia, F. Waldhauser, and G. C. Beroza (2004). Optimizing correlation techniques for improved earthquake location, *Bull. Seismol. Soc. Am.* **94**, 705–721, doi: [10.1785/0120040221](https://doi.org/10.1785/0120040221).
- Shearer, P. M., E. A. Abercrombie, D. T. Trugman, and W. Wang (2019). Comparing EGF methods for estimating corner frequency and stress drop from P wave spectra, *J. Geophys. Res.* **124**, no. 4, 3966–3986, doi: [10.1029/2018JB016957](https://doi.org/10.1029/2018JB016957).
- Sheen, D. -H. (2021). Analysis of the 2020 Haenam, Korea, earthquake sequence, *Geosci. J.* **25**, no. 1, 33–42, doi: [10.1007/s12303-020-0038-3](https://doi.org/10.1007/s12303-020-0038-3).
- Son, M., C. S. Cho, J. Choi, J. Jeon, and Y. K. Park (2021). Spatiotemporal patterns of the 2020 Haenam earthquake sequence, South Korea: lineament and migration implying fluid-driven earthquake swarm, *Geosci. J.* **25**, no. 1, 19–31, doi: [10.1007/s12303-020-0043-6](https://doi.org/10.1007/s12303-020-0043-6).
- Son, M., C. S. Cho, H. K. Lee, M. Han, J. S. Shi, K. Kim, and S. Kim (2020). Partitioned fault movement and aftershock triggering: evidence for fault interactions during the 2017 M_w 5.4 Pohang earthquake, *J. Geophys. Res.* **125**, no. 12, e2020JB020005, doi: [10.1029/2020JB020005](https://doi.org/10.1029/2020JB020005).

- Son, M., C. S. Cho, J. S. Shin, H. -M. Rhee, and D. -H. Sheen (2018). Spatiotemporal distribution of events during the first three months of the 2016 Gyeongju, Korea, earthquake sequence, *Bull. Seismol. Soc. Am.* **108**, no. 1, 210–217, doi: [10.1785/0120170107](https://doi.org/10.1785/0120170107).
- Son, M., J. S. Shin, G. Kim, and C. S. Cho (2015). Epicenter relocation of two 2013 earthquake sequences in the Yellow Sea, Korea, using travel-time double-differences and Lg-wave cross-correlation, *Geosci. J.* **19**, no. 2, 295–303, doi: [10.1007/s12303-014-0038-2](https://doi.org/10.1007/s12303-014-0038-2).
- Trugman, D. T. (2020). Stress-drop and source scaling of the 2019 Ridgecrest, California, earthquake sequence, *Bull. Seismol. Soc. Am.* **110**, no. 4, 1859–1871, doi: [10.1785/0120200009](https://doi.org/10.1785/0120200009).
- Trugman, D. T., and P. M. Shearer (2017). Applications of an improved spectral decomposition method to examine earthquake source scaling in southern California, *J. Geophys. Res.* **122**, no. 4, 2890–2910, doi: [10.1002/2017JB013971](https://doi.org/10.1002/2017JB013971).
- Trugman, D. T., Z. E. Ross, and P. A. Johnson (2020). Imaging stress and faulting complexity through earthquake waveform similarity, *Geophys. Res. Lett.* **47**, no. 1, e2019GL085888, doi: [10.1029/2019GL085888](https://doi.org/10.1029/2019GL085888).
- Uchide, T., and K. Imanishi (2016). Small earthquakes deviate from the omega-square model as revealed by multiple spectral ratio analysis, *Bull. Seismol. Soc. Am.* **106**, no. 3, 1357–1363, doi: [10.1785/0120150322](https://doi.org/10.1785/0120150322).
- Virtanen, P., R. Gommers, T. E. Oliphant, M. Haberland, T. Reddy, D. Cournapeau, E. Burovski, P. Peterson, W. Weckesser, J. Bright, S. J. van der Walt, *et al.* (2020). SciPy 1.0: Fundamental algorithms for scientific computing in python, *Nat. Methods* **17**, no. 3, 261–272, doi: [10.1038/s41592-019-0686-2](https://doi.org/10.1038/s41592-019-0686-2).
- Waldhauser, F., and D. P. Schaff (2008). Large-scale relocation of two decades of northern California seismicity using cross-correlation and double-difference methods, *J. Geophys. Res.* **113**, no. B8, doi: [10.1029/2007JB005479](https://doi.org/10.1029/2007JB005479).
- Waskom, M. L. (2021). Seaborn: Statistical data visualization, *J. Open Source Softw.* **6**, no. 60, 3021, doi: [10.21105/joss.03021](https://doi.org/10.21105/joss.03021).
- Wessel, P., J. F. Luis, L. Uieda, R. Scharroo, F. Wobbe, W. H. F. Smith, and D. Tian (2019). The Generic Mapping Tools version 6, *Geochem. Geophys. Geosys.* **20**, no. 11, 5556–5564, doi: [10.1029/2019GC008515](https://doi.org/10.1029/2019GC008515).
- Zaliapin, I., and Y. Ben-Zion (2013a). Earthquake clusters in southern California I: identification and stability, *J. Geophys. Res.* **118**, no. 6, 2847–2864, doi: [10.1002/jgrb.50179](https://doi.org/10.1002/jgrb.50179).
- Zaliapin, I., and Y. Ben-Zion (2013b). Earthquake clusters in southern California II: classification and relation to physical properties of the crust, *J. Geophys. Res.* **118**, no. 6, 2865–2877. doi: [10.1002/jgrb.50178](https://doi.org/10.1002/jgrb.50178).
- Zhang, J., X. Chen, and R. E. Abercrombie (2022). Spatiotemporal variability of earthquake source parameters at Parkfield, California, and their relationship with the 2004 M6 earthquake, *J. Geophys. Res.* **127**, no. 6, e2021JB022851, doi: [10.1029/2021JB022851](https://doi.org/10.1029/2021JB022851).

Manuscript received 25 June 2024

Published online 11 March 2025